Available online at www.sciencedirect.com
SCIENCE DIRECT®
Coastal Engineering 49 (2003) 99–124
Coastal Engineering
An International Journal for Coastal, Harbour and Offshore Engineers
www.elsevier.com/locate/coastaleng

A curvilinear version of a quasi-3D nearshore circulation model

Fengyan Shi[a,*], Ib A. Svendsen[a], James T. Kirby[a], Jane McKee Smith[b]

[a] *Ocean Engineering Laboratory, Center for Applied Coastal Research, University of Delaware, Newark, DE 19716, USA*
[b] *Engineer Research and Development Center, Coastal and Hydraulics Laboratory, 3909 Halls Ferry Road, Vicksburg, MS 39180, USA*

Received 31 May 2002; received in revised form 5 May 2003; accepted 4 June 2003

Abstract

A curvilinear version of the nearshore circulation model SHORECIRC is developed based on the quasi-3D nearshore circulation equations derived by Putrevu and Svendsen [Eur. J. Mech. 18 (1999) 409–427]. We use a generalized coordinate transformation and re-derive the equations in tensor-invariant forms. The contravariant component technique is used to simplify both the transformed equations and boundary conditions. A high-order finite-difference scheme with a staggered grid in the image domain is adopted for the numerical model. Very good convergence rates with both grid refinement and time refinement are obtained in a simple convergence test. The model is then applied to four cases involving either a non-orthogonal quadrilateral grid or a generalized curvilinear grid. The versatility of the curvilinear model in dealing with curved shorelines, nearshore breakwaters and other complicated geometries is demonstrated in the test cases. The accuracy of the model is shown in the paper through model/data comparisons in two of the case studies.

Keywords: Nearshore circulation model; Numerical model; Curvilinear coordinates; Finite difference method; Wave-induced circulation

1. Introduction

The performance of a numerical model for wave-induced nearshore circulation is important for predicting sediment and pollutant transport in coastal regions. The model performance mainly depends on the understanding of nearshore phenomena as well as numerical techniques used in the model. Over the last decades, significant progress has been made in our understanding of wave-generated phenomena such as wave set-up, wave breaking, undertow, cross-shore and longshore currents and their stability, turbulence and mixing, and the generation of long-wave phenomena. Based on this understanding, a variety of numerical models have been developed and used for modeling of nearshore phenomena.

Recently, the three-dimensional dispersion of momentum in wave-induced nearshore currents was discussed by Svendsen and Putrevu (1994). They found that the vertical nonuniformity of the currents leads to a mixing-like term in the depth-integrated alongshore momentum equation, which is analogous to the shear-dispersion mechanism found by Taylor (1953, 1954). The lateral mixing caused by the shear-dispersion mechanism is an order of magnitude larger than the turbulent lateral mixing and is thus considered to be a major contributor to the total lateral mixing in the nearshore region. Smith (1997) also presented a rather general derivation of the shear dispersion mechanism

* Corresponding author. Fax: +1-302-831-1228.
E-mail address: fyshi@coastal.udel.edu (F. Shi).

0378-3839/03/$ - see front matter © 2003 Elsevier B.V. All rights reserved.
doi:10.1016/S0378-3839(03)00049-8

for the case with no short-wave-induced volume flux. Putrevu and Svendsen (1999, PS99 hereafter) extended the results of Svendsen and Putrevu (1994) to the general case of unsteady circulations induced by wave breaking over an arbitrary bottom topography. For a zero wave-induced volume flux, the newly derived equations are similar to those of Smith. A quasi-3D numerical model named SHORECIRC (Svendsen et al., 2000) has been developed based on the nearshore circulation equations. It is a 2D horizontal model which incorporates the effect of the vertical structure of horizontal flows. A semi-analytical solution is used for the 3D current profiles in combination with a numerical solution for the depth-integrated 2D horizontal equations. Several applications of the model have been carried out in studies of various nearshore phenomena, such as surf-beat (Van Dongeren et al., 1995), longshore currents (Sancho et al., 1995), infragravity waves (Van Dongeren et al., 1996, 1998; Van Dongeren and Svendsen, 2000), shear waves (Sancho and Svendsen, 1998) and rip currents (Haas et al., 1998; Svendsen and Haas, 1999) and the model has been compared to data from the DELILAH field experiment (Svendsen et al., 1997).

The SHORECIRC model was developed in rectangular Cartesian coordinates and was only used in rectangular domains, thus limiting the applicability of the model to less complicated coastal environments. First, a rectangular grid is not able to fit complicated shoreline boundaries very well. Second, complicated geometries, such as harbors and tidal inlets, make the uniform-resolution model very expensive when a fine grid is used. Therefore, the development of a curvilinear version of SHORECIRC is necessary for its use in irregular shaped domains.

There are numerous examples of curvilinear grid methods in the study of waves and currents. Usually structured grid methods with finite-difference discretizations, or unstructured grid methods with a finite-element or finite-volume approach are used in model developments. Unstructured grids are more flexible than structured grids to fit complicated boundaries and are able to deal with very complex geometries. However, the finite-difference methods with structured curvilinear grids are much simpler to program than finite-element or finite-volume methods and thus are widely used in fluid dynamic fields. For example, Blumberg and Mellor (1987) developed a 3D coastal ocean circulation model (POM) in orthogonal curvilinear coordinates. Non-orthogonal boundary-fitted grid models with generalized coordinate transformation were developed by many authors (e.g., Sheng, 1986; Shi and Sun, 1995; Shi et al., 1997) for modeling coastal and estuarine processes.

For a generalized coordinate transformation, several advantages of using the contravariant technique have been recognized in the derivations of hyperbolic-type equations, as shown by Sheng (1986) and Shi and Sun (1995), among others. In generalized curvilinear coordinates, contravariant and covariant components are two kinds of vector components based on, respectively, a basis which is locally tangent to the curvilinear coordinate and a reciprocal basis which is locally normal to the curvilinear coordinate. The designation "contravariant" or "covariant" technique represents the choice of components which are adopted as primitive variables in the equations transformed from rectangular Cartesian coordinates. It has been found that both the contravariant technique and the covariant technique are able to simplify the transformed equations (see, for example, Warsi, 1998), in comparison to the Cartesian component method (see, for example, Häuser et al., 1985, 1986; Raghunath et al., 1987; Borthwick and Barber, 1992). The contravariant technique can simplify slip lateral boundary conditions compared to the covariant technique and is thus more conveniently used in hydrodynamic models with slip boundary conditions.

In the present paper, a curvilinear nearshore circulation model is developed based on the quasi-3D circulation equations. A generalized coordinate transformation and the contravariant technique are used in the model. Following the Cartesian version of the circulation model SHORECIRC (Svendsen et al., 2000), a fourth-order Adams–Bashforth–Moulton predictor–corrector scheme is employed in the curvilinear model to perform the time integration. Unlike the spatial discretization in the Cartesian version, we use a staggered grid system in the transformed image domain. A fourth-order scheme using standard five-point finite differencing is used in the first-order derivative terms, while a second-order scheme is used for the higher order derivatives and coordinate metrics for spatial discretizations. Various point types are defined in the model code to recognize different boundary conditions, which allows the model to be used in

complicated domains such as harbors and tidal inlets. We also test the numerical convergence, which is important for a curvilinear model. The model is finally applied to four cases involving either a nonorthogonal Cartesian grid or generalized curvilinear grid. The first case is the simulation of Gourlay's (1974) laboratory experiment in which currents were generated on a curved beach by diffracted waves in the lee of a breakwater. We generated a curvilinear grid to fit the curved beach. The breakwater is modeled with the recognition of point types. The second case is the simulation of longshore circulation around a conical island. A circular domain with curvilinear grid is employed for this case. The third case is the longshore current simulations for the longshore current experiment conducted at US Army Engineer Research and Development Center (Hamilton and Ebersole, 2001). A non-rectangular grid is employed to fit the oblique waveguides used in the physical experiment. The last case is a simulation of nearshore circulation at Grays Harbor, Washington. A curvilinear grid is generated to deal with the complicated geometry of jetties and an inlet.

This paper is organized as follows. First, we re-derive the circulation equations (PS99) in generalized curvilinear coordinates. Next, model implementations including numerical schemes, vertical profile calculations, as well as boundary conditions are described. Then, the numerical test on convergence and four model applications are carried out. The conclusions are drawn in the final section.

2. Derivations of equations in curvilinear coordinates

2.1. Coordinate transformation

A coordinate transformation is introduced in the general form

$$\begin{cases} \xi_1 = \xi_1(x_1, x_2) \\ \xi_2 = \xi_2(x_1, x_2) \\ z = z \end{cases} \tag{1}$$

where (x_1, x_2, z) are spatial independent variables in rectangular Cartesian coordinates and (ξ_1, ξ_2, z) are new independent variables in the transformed image domain. z represents the vertical coordinate. Any vector $\mathbf{v}$ can be written in Cartesian coordinates as

$$\mathbf{v} = v_1\mathbf{i} + v_2\mathbf{j} + v_3\mathbf{k} \tag{2}$$

where ($\mathbf{i}$, $\mathbf{j}$, $\mathbf{k}$) are Cartesian basis vectors. In the generalized curvilinear coordinates, the coordinate basis is the combination of the generalized horizontal basis ($\mathbf{a}_1$, $\mathbf{a}_2$) and the vertical Cartesian base vector $\mathbf{k}$ and is written as ($\mathbf{a}_1$, $\mathbf{a}_2$, $\mathbf{k}$). Using the new basis ($\mathbf{a}_1$, $\mathbf{a}_2$, $\mathbf{k}$), the vector $\mathbf{v}$ can be described as

$$\mathbf{v} = v^{\alpha}\mathbf{a}_{\alpha} + v_3\mathbf{k} \quad (\alpha = 1, 2) \tag{3}$$

where v^{α} are contravariant horizontal components of the vector; v_3 is the vertical Cartesian component of the vector.

The relationship between horizontal components in the Cartesian and contravariant components in the curvilinear coordinates may be written as

$$v^{\alpha} = \frac{\partial \xi_{\alpha}}{\partial x_{\beta}} v_{\beta} \quad (\alpha, \beta = 1, 2) \tag{4}$$

where v_{β} represents the Cartesian components.Following the velocity splitting method in PS99, the contravariant components of instantaneous horizontal velocity can be written as

$$u^{\alpha} = u'^{\alpha} + u_w^{\alpha} + \tilde{V}^{\alpha} + V_1^{\alpha} \tag{5}$$

where u'^{α}, u_w^{α}, $\tilde{V}^{\alpha}$, and V_1^{α} are, respectively, the turbulence component, the wave component, the component of depth-averaged and short-wave-averaged velocity, and the vertical variation of the short-wave-averaged velocity.

2.2. Depth-integrated, short-wave-averaged equations

The model equations in PS99 were derived in rectangular Cartesian coordinates and described in terms of Cartesian tensor representations. It may not be appropriate if we only transform the final Eqs. (4) and (45) in PS99 from Cartesian coordinates into curvilinear coordinates since use of the direct transformation does not allow a simplification of the equations using the contravariant technique. In addition, we can not guarantee that the curvilinear counter-

parts of the 3D coefficients M, A, D and B in PS99) are in correct form after the generalized coordinate transformation. Therefore, we re-derive the equations in generalized coordinates, starting with the depth-integrated, short-wave-averaged equations as shown in Eqs. (4) and (5) in PS99.

The depth-integrated, short-wave-averaged continuity equation (PS99, Eq. (4)) in terms of contravariant components is given by

$$\frac{\partial \bar{\zeta}}{\partial t} + \frac{1}{\sqrt{g_0}} \frac{\partial}{\partial \xi_\alpha} (\sqrt{g_0} \tilde{V}^\alpha h) = 0 \tag{6}$$

where g_0 is the determinant of the metric tensor $g_{\alpha\beta}$,

$$g_0 = \begin{vmatrix} g_{11} & g_{12} \\ g_{21} & g_{22} \end{vmatrix} \tag{7}$$

in which

$$g_{\alpha\beta} = \frac{\partial x_\gamma}{\partial \xi_\alpha} \frac{\partial x_\gamma}{\partial \xi_\beta} \tag{8}$$

To get Eq. (6), we start with the general form of the continuity equation and then write it in a tensor-invariant form that can be simplified to the contravariant component equation. The detailed derivation of Eq. (6) can be found in Appendix A.

Similarly, the depth-integrated, short-wave-averaged momentum equation can be written in terms of contravariant components as

$$\begin{aligned} &\frac{\partial}{\partial t}(\tilde{V}^\alpha h) + \left[\tilde{V}^\alpha \tilde{V}^\beta h + \int_{-h_0}^{\bar{\zeta}} V_1^\alpha V_1^\beta \mathrm{d}z + Q_w^\alpha V_1^\beta(\bar{\zeta}) \right. \\ &\left. + V_1^\alpha(\bar{\zeta}) Q_w^\beta \right]_{,\beta} + \frac{1}{\rho} T_{,\beta}^{\alpha\beta} + \frac{1}{\rho} S_{,\beta}^{\alpha\beta} + gh \frac{\partial \zeta}{\partial \xi_\beta} g^{\beta\alpha} \\ &- \frac{1}{\rho} \tau_s^\alpha + \frac{1}{\rho} \tau_{\mathrm{B}}^\alpha = 0 \end{aligned} \tag{9}$$

where Q_w^α represents the contravariant components of short-wave-induced volume flux as defined in PS99. $g^{\beta\alpha}$ are the contravariant metric defined as

$$g^{\beta\alpha} = \frac{\partial \xi_\alpha}{\partial x_\gamma} \frac{\partial \xi_\beta}{\partial x_\gamma}. \tag{10}$$

τ_{s}^α and τ_{B}^α are the contravariant components of the surface shear stress and the bottom shear stress, respectively. $S^{\alpha\beta}$ and $T^{\alpha\beta}$ are the contravariant components of the short-wave-induced radiation stress tensor and the depth-integrated Reynolds' stress tensor, respectively. $()_{,\beta}^{\alpha\beta}$ presents the covariant derivative of a second-order tensor, given by

$$T_{,\beta}^{\alpha\beta} = \frac{1}{\sqrt{g_0}} \frac{\partial \sqrt{g_0} T^{\alpha\beta}}{\partial \xi_\beta} + T^{\gamma\beta} \Gamma_{\gamma\beta}^\alpha \tag{11}$$

where $\Gamma_{\gamma\beta}^\alpha$ is Christoffel symbol of the second kind. The detailed derivation of Eq. (9) and calculations of $T_{,\beta}^{\alpha\beta}$ and $S_{,\beta}^{\alpha\beta}$ can be found in Appendix A.

In (9), $\int_{-h_0}^{\bar{\zeta}} V_1^\alpha V_1^\beta \mathrm{d}z + Q_w^\alpha V_1^\beta(\bar{\zeta}) + V_1^\alpha(\bar{\zeta}) Q_w^\beta$ represents the effects of the vertical nonuniformity of the short-wave-averaged velocities and give rise to the dispersive mixing as described in PS99. These terms are evaluated using the solution for V_1^α.

2.3. Solution for V_1^α

To get the solution for V_1^α, we start with the horizontal momentum equation as in PS99. The following tensor-invariant form of the equation is obtained from the general form of the Eq. (55) shown in Appendix A.

$$\frac{\partial u^\alpha}{\partial t} + (u^\alpha u^\beta)_{,\beta} + \frac{\partial}{\partial z}(u^\alpha w) = -\frac{1}{\rho} \frac{\partial p}{\partial \xi_\beta} g^{\beta\alpha} \tag{12}$$

where p is the instantaneous pressure; w is the vertical component of the instantaneous velocity. Introducing Eq. (5) into Eq. (12) and averaging over a wave period leads to

$$\begin{aligned} &\frac{\partial V_1^\alpha}{\partial t} + \frac{\partial \tilde{V}^\alpha}{\partial t} + \left(V_1^\alpha V_1^\beta + \tilde{V}^\alpha \tilde{V}^\beta + V_1^\alpha \tilde{V}^\beta + V_1^\beta \tilde{V}^\alpha \right. \\ &\left. + \overline{u_w^\alpha u_w^\beta} + \overline{u'^\alpha u'^\beta} \right)_{,\beta} + \frac{\partial}{\partial z} \left(V_1^\alpha W + \tilde{V}^\alpha W \right. \\ &\left. + \overline{u_w^\alpha w_w} + \overline{u'^\alpha w'} \right) = -\frac{1}{\rho} \frac{\partial \bar{p}}{\partial \xi_\beta} g^{\beta\alpha} \end{aligned} \tag{13}$$

where W represents the vertical component of the time averaging velocity. Assuming hydrostatic pressure and

the eddy viscosity closure (see Appendix A), we get the tensor-invariant form of PS99 (Eq. (16))

$$\begin{aligned}\frac{\partial V_1^\alpha}{\partial t}-\frac{\partial}{\partial z}\left(\nu_t\frac{\partial V_1^\alpha}{\partial z}\right)&=-\left(\frac{\partial \tilde{V}^\alpha}{\partial t}+\tilde{V}^\beta\tilde{V}^\alpha_{,\beta}+gg^{\beta\alpha}\frac{\partial\bar{\zeta}}{\partial\xi_\beta}+f^\alpha\right)\\&\quad-\left(\tilde{V}^\beta V^\alpha_{1,\beta}+V_1^\beta\tilde{V}^\alpha_{,\beta}+V_1^\beta V^\alpha_{1,\beta}+W\frac{\partial V_1^\alpha}{\partial z}\right)\\&\quad+\left[\nu_t(g^{\gamma\beta}V^\alpha_{,\gamma}+g^{\gamma\alpha}V^\beta_{,\gamma})\right]_{,\beta}+\frac{\partial}{\partial z}\left(\nu_t g^{\beta\alpha}\frac{\partial W}{\partial\xi_\beta}\right)\end{aligned}\tag{14}$$

where

$$f^\alpha=\left(\overline{u_w^\alpha u_w^\beta}\right)_{,\beta}+\frac{\partial\left(\overline{w_w u_w^\alpha}\right)}{\partial z}-g^{\beta\alpha}\frac{\partial\overline{w_w w_w}}{\partial\xi_\beta}\tag{15}$$

and $()^\alpha_\beta$ represents the covariant derivative of a first-order tensor defined by Eq. (43).Using the continuity equation (Eq. (6)), the depth-integrated momentum Eq. (9) may be written as

$$\begin{aligned}\frac{\partial\tilde{V}^\alpha}{\partial t}+\tilde{V}^\beta\tilde{V}^\alpha_{,\beta}+gg^{\beta\alpha}\frac{\partial\bar{\zeta}}{\partial\xi_\beta}&=-\frac{1}{\rho h}S^{\alpha\beta}_{,\beta}-\frac{1}{\rho h}\tau_{\mathrm{B}}^\alpha-\frac{1}{\rho h}T^{\alpha\beta}_{,\beta}-\frac{1}{h}\\&\quad\times\left(\int_{-h}^{\bar{\zeta}}V_1^\alpha V_1^\beta\mathrm{d}z+Q_w^\alpha V_1^\beta(\bar{\zeta})+V_1^\alpha(\bar{\zeta})Q_w^\beta\right)_{,\beta}\end{aligned}\tag{16}$$

Eq. (16) can be used to rewrite Eq. (14) as

$$\begin{aligned}\frac{\partial V_1^\alpha}{\partial t}-\frac{\partial}{\partial z}(\nu_t\frac{\partial V_1^\alpha}{\partial z})&=\left(\frac{1}{\rho h}S^{\alpha\beta}_{,\beta}-f^\alpha+\frac{\tau_{\mathrm{B}}^\alpha}{\rho h}\right)\\&\quad-\left(\tilde{V}^\beta V^\alpha_{1,\beta}+V_1^\beta\tilde{V}^\alpha_{,\beta}+V_1^\beta V^\alpha_{1,\beta}+W\frac{\partial V_1^\alpha}{\partial z}\right)\\&\quad-\frac{1}{h}\left(\int_{-h}^{\bar{\zeta}}V_1^\alpha V_1^\beta\mathrm{d}z+Q_w^\alpha V_1^\beta(\bar{\zeta})+V_1^\alpha(\bar{\zeta})Q_w^\beta\right)_{,\beta}\\&\quad+\left\{\left[\nu_t(g^{\gamma\beta}V^\alpha_{,\gamma}+g^{\gamma\alpha}V^\beta_{,\gamma})\right]_{,\beta}\right.\\&\quad\left.+\frac{\partial}{\partial z}\left(\nu_t g^{\beta\alpha}\frac{\partial W}{\partial\xi^\beta}\right)+\frac{1}{\rho h}T^{\alpha\beta}_{,\beta}\right\}\end{aligned}\tag{17}$$

By comparing Eq. (17) against PS99, Eq. (19), the major changes of the equation after the transformation can be found that the regular horizontal derivatives in the Cartesian equation become the covariant derivatives in the generalized curvilinear equation. The vertical derivative terms in the generalized equation appear to be in the same form as that in the Cartesian equation since there is no transformation in the vertical direction. Therefore, the solution for V_1^α should be in the same form as in Cartesian coordinates as described below.

After the non-dimensional analysis and perturbation as in PS99, we use a perturbation expansion of the type

$$V_1^\alpha=V_1^{\alpha(0)}+\delta V_1^{\alpha(1)}+\ldots\tag{18}$$

where δ (~ 0.1) represents the size of the short-wave-induced quantities; $V_1^\alpha(0)$ and $V_1^\alpha(1)$ represent zero- and first-order of the contravariant components. We only consider the first two terms on the right hand side of (18) in the present paper. The governing equation for $V_1^{\alpha(0)}$ is

$$\frac{\partial V_1^{\alpha(0)}}{\partial t}-\frac{\partial}{\partial z}\left(\nu_t\frac{\partial V_1^{\alpha(0)}}{\partial z}\right)=F^\alpha\tag{19}$$

where

$$F^\alpha=\frac{1}{\rho h}S^{\alpha\beta}_{,\beta}-f^\alpha+\frac{\tau_{\mathrm{B}}^\alpha}{\rho h}\tag{20}$$

The solution for $V_1^{\alpha(0)}$ will be the same as the solution in Cartesian coordinates (PS99, Eqs. (34) and (37)) except the solution value represents the contravariant component of the vector.

Similarly, the solution for $V_1^{\alpha(0)}$ can be written in the same form as in PS99, Eq. (42) except that

$$\begin{aligned}R_\alpha^{(1)}(z,t)=-\left(\tilde{V}^\beta V^{\alpha(0)}_{1,\beta}+V_1^{\beta(0)}\tilde{V}^\alpha_{,\beta}+V_1^{\beta(0)}V^{\alpha(0)}_{1,\beta}\right.\\\left.+W\frac{\partial V_1^{\alpha(0)}}{\partial z}\right)+\frac{1}{h}\left(\int_{-h}^{\bar{\zeta}}V_1^{\alpha(0)}V_1^{\beta(0)}\mathrm{d}z\right.\\\left.+Q_w^\alpha V_1^{\beta(0)}(\bar{\zeta})+V_1^{\alpha(0)}(\bar{\zeta})Q_w^\beta\right)_{,\beta}\end{aligned}\tag{21}$$

2.4. Results for the integrals

The derivation for the integrals required in Eq. (9) is very similar to that in PS99, noticing that all the horizontal derivatives in PS99 should be replaced by the corresponding covariant derivatives in generalized coordinates.

In PS99, Eq. (94) was used to replace W in PS99, Eq. (93). The representation of W in general coordinates may be written as

$$W = -\left[(\tilde{V}^{\beta} + V_1^{\beta(0)}(-h_0))\frac{\partial h_0}{\partial x_{\beta}} + (h_0 + z)\tilde{V}^{\beta}_{,\beta} + \int_{-h_0}^{z} V_{1,\beta}^{\beta(0)}\mathrm{d}z\right]. \tag{22}$$

In the derivation of Eq. (22), we use the following relations:

$$\begin{aligned} W &= -\left(\int_{-h_0}^{z} V^{\beta}\mathrm{d}z\right)_{,\beta} \\ &= \frac{\partial \int_{-h_0}^{z} V^{\beta}\mathrm{d}z}{\partial \xi_{\beta}} + \int_{-h_0}^{z} V^{\alpha}\mathrm{d}z\Gamma^{\beta}_{\beta\alpha} \\ &= \int_{-h_0}^{z} \frac{\partial V^{\beta}}{\partial \xi_{\beta}}\mathrm{d}z + V^{\beta}(-h_0)\frac{\partial h_0}{\partial \xi_{\beta}} + \int_{-h_0}^{z} V^{\alpha}\Gamma^{\beta}_{\beta\alpha}\mathrm{d}z \\ &= \int_{-h_0}^{z} V^{\beta}_{,\beta}\mathrm{d}z + V^{\beta}(-h_0)\frac{\partial h_0}{\partial \xi_{\beta}} \end{aligned} \tag{23}$$

Following the steps in PS99 leads to the results for the integrals in Eq. (16) in general coordinates:

$$\begin{aligned} &\int_{-h_0}^{\bar{\zeta}} V_1^{\alpha}V_1^{\beta}\mathrm{d}z + Q_w^{\alpha}V_1^{\beta}(\bar{\zeta}) + V_1^{\alpha}(\bar{\zeta})Q_w^{\beta} \\ &\quad = M_{\alpha\beta} + A_{\alpha\beta\delta}\tilde{V}^{\delta} - h(D_{\delta\beta}\tilde{V}^{\alpha}_{,\delta} + D_{\delta\alpha}\tilde{V}^{\beta}_{,\delta} + B_{\alpha\beta}\tilde{V}^{\delta}_{,\delta}) \end{aligned} \tag{24}$$

The final tensor form of the momentum Eq. (16) (similar to PS99, Eq. (45)) can be written as

$$\begin{aligned} &\frac{\partial}{\partial t}(\tilde{V}^{\alpha}h) + (\tilde{V}^{\alpha}\tilde{V}^{\beta}h + A_{\alpha\beta\delta}\tilde{V}^{\delta})_{,\beta} + \frac{1}{\rho}(S^{\alpha\beta} + \rho M_{\alpha\beta})_{,\beta} \\ &\quad + ghg^{\beta\alpha}\frac{\partial \bar{\zeta}}{\partial \xi_{\beta}} + \frac{\tau_B^{\alpha}}{\rho} + [T^{\alpha\beta} - h(D_{\delta\beta}\tilde{V}^{\alpha}_{,\delta} + D_{\delta\alpha}\tilde{V}^{\beta}_{,\delta})]_{,\beta} \\ &\quad - (hB_{\alpha\beta}\tilde{V}^{\delta}_{,\delta})_{,\beta} = 0 \end{aligned} \tag{25}$$

where the tensors A, B, D and M have the same definitions as in PS99 except all the horizontal derivatives of $V_1^{(0)}$ should be replaced by the corresponding covariant derivatives.

Expanding the covariant derivatives in Eq. (25), the momentum equations in generalized curvilinear coordinates can also be written as

$$\begin{aligned} &\frac{\partial}{\partial t}(\tilde{V}^{\alpha}h) + \frac{1}{\sqrt{g_0}}\frac{\partial}{\partial \xi_{\beta}}[\sqrt{g_0}(\tilde{V}^{\alpha}\tilde{V}^{\beta}h + A_{\alpha\beta\delta}\tilde{V}^{\delta})] \\ &\quad + (\tilde{V}^{\gamma}\tilde{V}^{\beta}h + A_{\gamma\beta\delta}\tilde{V}^{\delta})\Gamma^{\alpha}_{\gamma\beta} + \frac{1}{\rho\sqrt{g_0}}\frac{\partial}{\partial \xi_{\beta}} \\ &\quad \times [\sqrt{g_0}(S^{\alpha\beta} + \rho M_{\alpha\beta})] + \frac{1}{\rho}(S^{\gamma\beta} + \rho M_{\gamma\beta})\Gamma^{\alpha}_{\gamma\beta} \\ &\quad + ghg^{\beta\alpha}\frac{\partial \bar{\zeta}}{\partial \xi_{\beta}} + \frac{\tau_B^{\alpha}}{\rho} + \frac{1}{\sqrt{g_0}}\frac{\partial}{\partial \xi_{\beta}}\{\sqrt{g_0}[T^{\alpha\beta} \\ &\quad - h(D_{\delta\beta}\tilde{V}^{\alpha}_{,\delta} + D_{\delta\alpha}\tilde{V}^{\beta}_{,\delta})]\} + [T^{\gamma\beta} - h(D_{\delta\beta}\tilde{V}^{\gamma}_{,\delta} \\ &\quad + D_{\delta\gamma}\tilde{V}^{\beta}_{,\delta})]\Gamma^{\alpha}_{\gamma\beta} - \frac{1}{\sqrt{g_0}}\frac{\partial}{\partial \xi_{\beta}}[\sqrt{g_0}(hB_{\alpha\beta}\tilde{V}^{\delta}_{,\delta})] \\ &\quad - (hB_{\gamma\beta}\tilde{V}^{\delta}_{,\delta})\Gamma^{\alpha}_{\gamma\beta} = 0 \end{aligned} \tag{26}$$

Eqs. (6) and (26) are the nearshore circulation equations in generalized curvilinear coordinates.

3. Model implementation

3.1. Numerical scheme

Following the Cartesian version of the SHORECIRC model, the governing equations (Eqs. (6) and (26)) are solved using the fourth-order Adams–Bashforth–Moulton predictor–corrector scheme to per-

form the time integration. A fourth-order scheme using standard five-point finite differencing is used for the first-order spatial derivative terms and a second-order central scheme is used for higher order derivatives, metric tensors and Christoffel symbols. In contrast to the non-staggered grid used in the Cartesian version, we employ a staggered grid in the (ξ_1, ξ_2) plane with which the numerical noise level was found to become lower than that with a non-staggered grid. The staggered grid arrangement and the detailed numerical schemes can be found in Appendix C. In addition, various point types are defined on the staggered grid to recognize different boundary conditions and to deal with complicated structures in a computational domain. No numerical filtering is needed in the code.

3.2. Calculation of vertical current profiles

As described in Eq. (18), the depth-varying current velocity is split into two parts. The first part $V_1^{\alpha(0)}$ is primarily the component generated by the local external forcing F^α in Eq. (20) while the second part $V_1^{\alpha(1)}$ is generated by the advective terms shown in Eq. (17). After a scale analysis in PS99, a reasonable assumption is made that the first component is much larger than the second one. In addition, the expressions of coefficients A, B, D and M in PS99 also show that the contributions to these coefficients from $V_1^{\alpha(1)}$ can be expressed in terms of the $V_1^{\alpha(0)}$ component in the values of the current–current and current–wave interaction terms. Therefore, we only use $V_1^{\alpha(0)}$ to present the vertical variation of V_1^α. $V_1^{\alpha(0)}$ is given by

$$V_1^{\alpha(0)} = d_{1\alpha}\xi^2 + e_{1\alpha}\xi + f_{1\alpha} + f_{2\alpha} \tag{27}$$

where

$$\xi = z + h \tag{28}$$

in which h is the water depth from the mean water level to the bottom. In Eq. (27)

$$d_{1\alpha} = \frac{1}{2\nu_t}\left[\frac{1}{\rho h}((\nabla\cdot\mathbf{S})^\alpha + \tau_B^\alpha - \tau_{ss}^\alpha) - f_\alpha\right] \tag{29}$$

where $(\nabla\cdot\mathbf{S})^\alpha$ is contravariant component of $\nabla\cdot\mathbf{S}$; τ_{ss}^α represents the shear stress associated with the steady streaming and f_α represents the short-wave forcing (see Putrevu and Svendsen, 1995 for detail).

$$e_{1\alpha} = \frac{\tau_B^\alpha - \tau_{ss}^\alpha}{\nu_t} \tag{30}$$

$$f_{1\alpha} + f_{2\alpha} = -\frac{Q_w^\alpha}{h} - \frac{h(\tau_B^\alpha - \tau_{ss}^\alpha)}{2\rho\nu_t} - \frac{1}{3}d_{1\alpha}h^2 \tag{31}$$

Substituting Eq. (27) into the integration forms of the coefficients A, B, D and M in PS99, we can get the final expressions of the dispersive mixing coefficients as shown in Appendix B.

3.3. Boundary conditions

There are several types of boundary conditions implemented in the curvilinear model. First, slip boundary conditions can be used for lateral walls, shorelines and boundaries of structures inside a computational domain. As mentioned in the introduction of the paper, the contravariant technique can simplify the expressions of slip boundary conditions in curvilinear coordinates. For a curvilinear boundary, the slip boundary condition can be simply expressed as

$$\tilde{V}^\alpha = 0. \tag{32}$$

Second, a specified-flux boundary condition is implemented by using the contravariant component. The contravariant component of the specified velocity (or flux) can be obtained using the transformation relation (Eq. (4)).

Third, a periodic boundary condition along cross-shore boundaries at the two ends of the domain is also an option in this model for simulations of uniform beaches. The implementation of the periodic boundary condition is similar to that in the Cartesian version of the SHORECIRC model except that all vector variables are taken in contravariant forms. The periodic boundary condition requires both the bathymetry and grid to be periodic.

4. Numerical test and application

4.1. Convergence test

Convergence is a very important numerical property for a curvilinear model since variable grid spacing is

generally used in a grid system. As a simple test case (Shi et al., 2001), the evolution of waves in a rectangular basin is calculated to test the convergence with both space and time discretization.

The basin dimensions are 20 × 20 m, and the water depth is 0.5 m constant over the basin. The initial condition is provided by a motionless Gaussian hump of water with its center located at the center of the basin (x_c, y_c):

$$\zeta(x,y,t=0)=H_0\exp\{-\gamma[(x-x_c)^2+(y-y_c)^2]/L^2\}, \tag{33}$$

$$u(x,y,t=0)=0, \tag{34}$$

$$v(x,y,t=0)=0, \tag{35}$$

where H_0 is the initial height of the hump; L is a scale length; γ is the shape coefficient, and (x_c, y_c) is the coordinate at the center of the domain. We chose $H_0=0.2$ m, $L=1$ m, $\gamma=0.4$, and $x_c=y_c=10$ m.

To test the grid convergence, we keep the time step as a constant, i.e., $\Delta t=0.01$ s, and adopt a sequence of different grid spacing $\Delta x\times p$, where $\Delta x=0.05$ m and $p=1,2,\ldots,8$ (The Courant Numbers are less than 0.5 in all the cases). Fig. 1 shows the convergence rate with grid refinement that is demonstrated by the RMS differences of simulated surface elevations at $t=10$ s. The RMS difference of surface elevation is defined by

$$\mathrm{RMS}_p=\sqrt{\frac{\sum_{i=1}^{m}\sum_{j=1}^{n}(\zeta_p(i,j)-\zeta_{p+1}(i,j))^2}{m\times n}} \tag{36}$$

where ζ_p represents the calculated surface elevations in the case p. (m, n) are the grid dimensions in the case of $p=8$. Fig. 1 shows that the logarithmic RMS differences decrease linearly when grid spacing decrease. Then, the Cauchy convergence rate defined by the following formula can be calculated.

$$R=\frac{\log(\mathrm{RMS}_p/\mathrm{RMS}_{p+1})}{\log(\Delta x_p/\Delta x_{p+1})} \tag{37}$$

The averaged R calculated in this case is 3.58 which is very reasonable since both fourth-order and second-order schemes are utilized in the model.

Similarly, the convergence with time discretization is examined by using a sequence of time steps from 0.004 to 0.02 s and keeping a constant grid spacing $\Delta x=0.2$ m. The convergence rate with time step refinement is shown in Fig. 2. The averaged convergence rate is 2.32 which is a little lower than the grid spacing convergence rate. It is found that the time refinement convergence rate can be improved to about 3.0 by using an under-relaxed iteration technique (Wei and Kirby, 1995) during the corrector stage in the code. We do not use the iteration technique for computational economy and assume the convergence rate without iteration to be sufficient for the model.

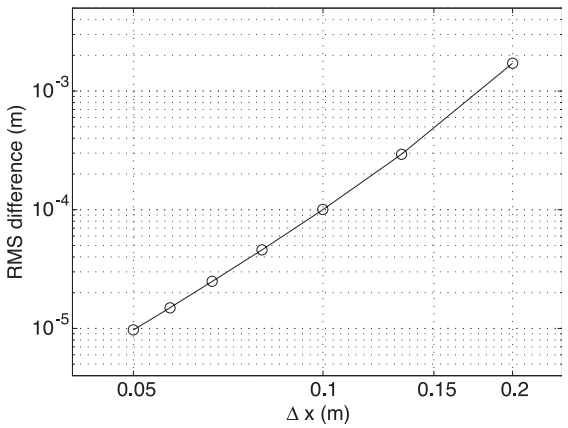

Fig. 1. Convergence rates with grid refinement.

4.2. Simulation of laboratory experiment of Gourlay

Gourlay (1974) carried out a laboratory experiment in which currents were generated on a curved beach by diffracted waves in the lee of a breakwater. The purpose of the experiment was to demonstrate that longshore variation of the wave height could generate longshore currents. Fig. 3 shows the laboratory setup for Gourlay's experiment. A 1 on 10 concrete beach is parallel to the incoming wave crests in the exposed zone. In the shadow zone, the slope is also 1/10 towards the curved beach which has a constant radius centered on the breakwater tip. The

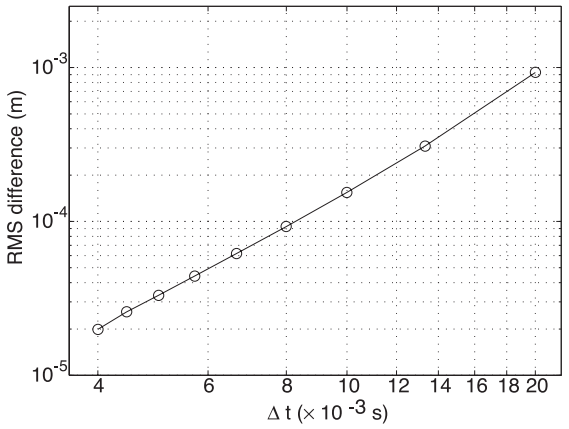

Fig. 2. Convergence rates with time step refinement.

wave basin was thus designed so that the shoreline was everywhere approximately parallel with the diffracted wave crests.

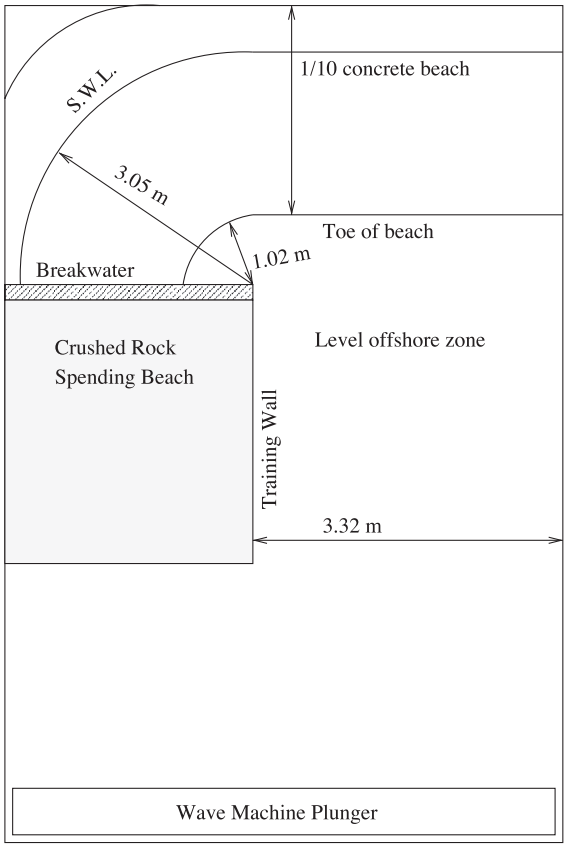

Fig. 3. Layout of Gourlay's experiment.

Winer (1988) employed a numerical model to simulate Gourlay's laboratory experiment. He used REF/DIF-1 (Kirby et al., 2002) as the wave driver and used depth-averaged shallow water equations which include radiation stress terms in the circulation model. Because a Cartesian coordinate system was adopted in the numerical model, a stair-type boundary was employed at the curved beach. This boundary effect was shown in the contour plots of both wave set-up and velocity amplitude in his results.

We use the present curvilinear model to simulate the experiment. A curvilinear grid shown in Fig. 4 is used to fit the curved shoreline boundary. Rather than the small computational domain Winer chose from the shoreline to 3 m offshore of the breakwater, a larger computational domain including the wave paddle area is employed to provide enough reservoir to feed the wave set-up, as in the laboratory experiment. The grid sizes are about 0.1 m in the offshore region and the exposed straight shoreline region and less than 0.1 m around the curved beach.

REF/DIF-1 is used as the wave-driver in a subroutine of the model code and provides the circulation model with radiation stresses, short-wave-induced volume flux, breaking wave energy dissipation, and

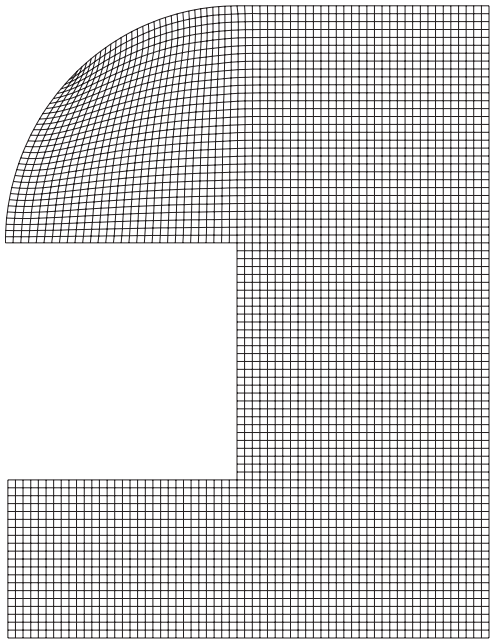

Fig. 4. Computational grid for simulation of Gourlay's experiment.

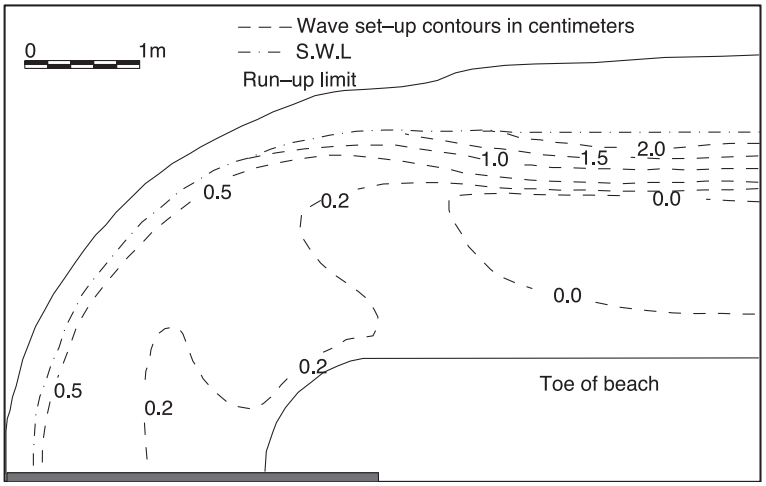

Fig. 5. Wave set-up contours from Gourlay's experiment (from Gourlay, 1974).

wave bottom velocity. Because REF/DIF-1 is operating in a Cartesian grid, an interpolation is needed for the data transfer from the Cartesian grid to the curvilinear grid (see Appendix D for detail). In REF/DIF-1, the wet and dry grid technique proposed by Kirby and Dalrymple (1986) is used for treating the dry grid points as though they have a very small depth of water (1 mm in the present paper). A wave height of 9.1 cm with a wave period of 1.5 s is used in REF/DIF-1 as the incident wave conditions, as in Winer's simulation.

The bottom stress formulation (Svendsen et al., 2000) with a constant bottom friction coefficient $f_{cw}=0.008$ is adopted in the case. The turbulence mixing coefficients in the eddy viscosity formulation are chosen as the same values as in Svendsen et al. (2000). The coefficients are also used in the following laboratory experiment cases.

Figs. 5 and 6 show the experimental results for the mean water surface contours and the corresponding results obtained from the numerical model, respectively. The comparison demonstrates that the numerical results agree very well with the experiment results. In contrast to Winer's results, which failed to show any set-up in the area of the connection of the shoreline and

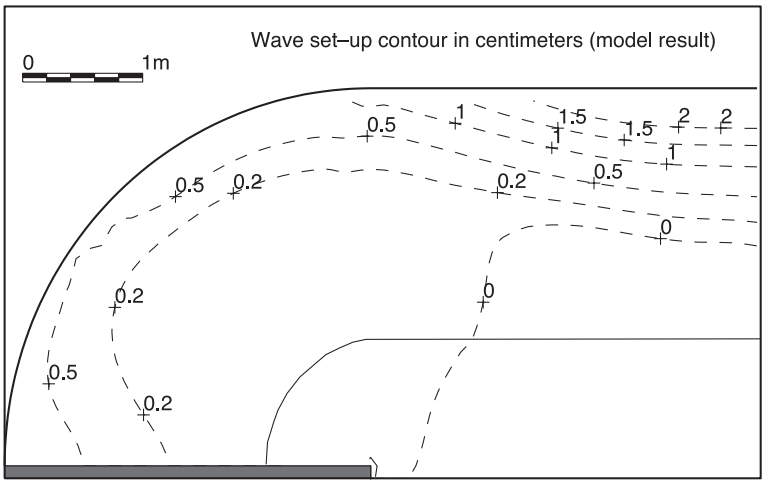

Fig. 6. Wave set-up contours from numerical results.

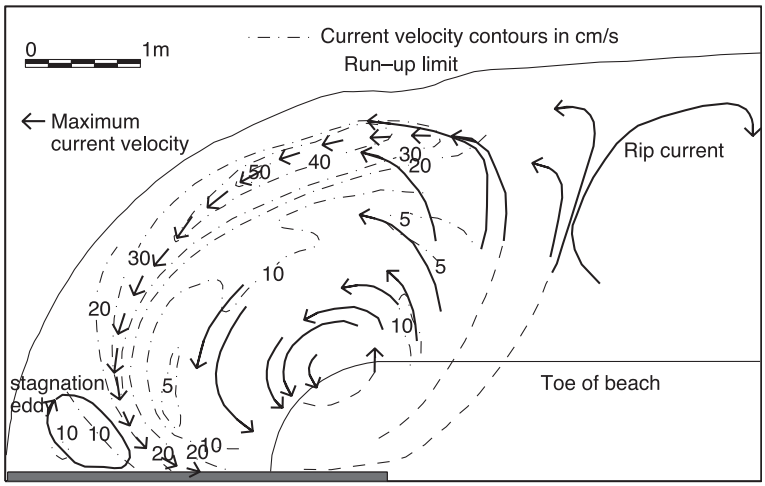

Fig. 7. Contours of current velocities and streamlines from Gourlay's experiment (from Gourlay, 1974).

the breakwater, the present model results show a wave set-up in this region which is consistent with the laboratory results.

To make model/data comparisons for the circulation, we present Gourlay's experimental results in Fig. 7. The figure illustrates both the contours for the magnitude of the velocity and some streamlines indicating the direction of the flow. The corresponding results from the numerical model are shown in Fig. 8. It can be seen from the comparison that the overall agreement is fairly good. Both the magnitude and the locations of the maximum currents obtained in the numerical model are similar to that in the laboratory experiment. The shoreward oriented current in the area directly exposed to the incident waves is very well shown in the numerical results. The present model also predicts the location of the primary eddy center and current magnitude behind the breakwater as shown in Fig. 8. However, the model fails to predict the stagnation eddy in the corner behind the breakwater although it does provide the set-up variation in that area as shown in Fig. 6. The parabolic wave model is suspected responsible to cause the discrepancy because it is not appropriate model in predicting wave diffraction

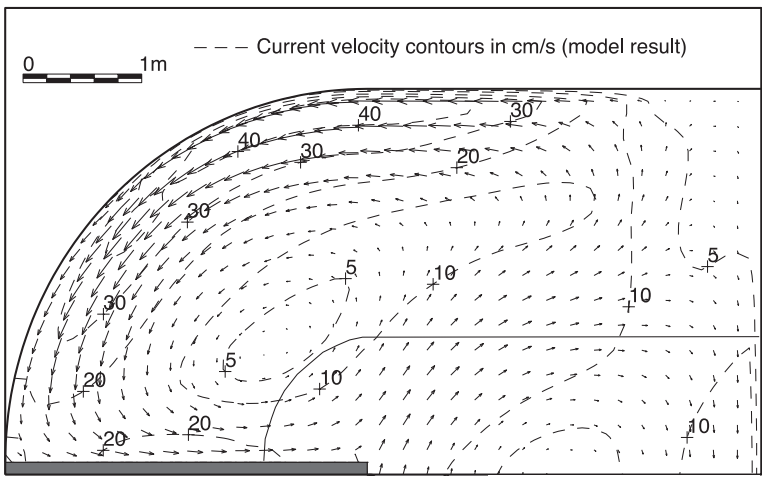

Fig. 8. Contours of current velocities and velocity vectors from numerical results.

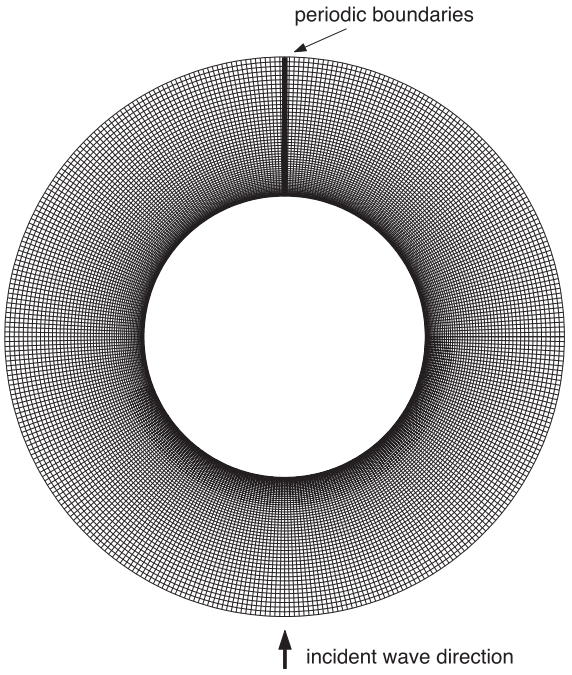

Fig. 9. Computational grid for simulation of longshore circulation around a conical island.

in the sheltered region. Further studies using other wave models may be needed to precisely simulate this phenomena.

4.3. Longshore circulation around a Conical Island

Mei and Angelides (1977) conducted a semi-theoretical study of the averaged circulation caused by waves breaking on the constant slope beach around a circular island in a sea of constant depth. They used the geometric refraction method and the energy conservation theory for wave calculations. For calculations of circulation, they used very simple depth-and time-averaged equations of motion that include pressure gradient, radiation stress and bottom friction terms. Polar coordinates were used in the circulation model. They concluded that the wave refraction pattern determines the extent of longshore circulation. In particular, for an island so large that there is a lee shore which is not affected by the refracting waves, two current cells are found on two sides of the island with respect to the wave direction, without significant penetration in the lee shore region. This conclusion was used to explain the creation of two sand spits for abrasive island shores.

As a simple and efficient case for testing the coordinate transformation within a circular domain, the so-called ‘large island’ case is carried out in the present paper as in Mei and Angelides (1977). The radius of the island is 3048 m (10,000 ft). The water depth of the flat seabed is 30.48 m (100 ft) and the beach slope we adopted in the simulation is 1/40. The incident wave height and wave period are, respectively, 6 m and 10 s. REF/DIF-1 is again used for wave calculation and the wet and dry grid technique is also used to deal with the island geometry.

Fig. 9 shows the computational grid generated according to the following formula:

$$x(i,j) = [3048 + 15(i-1) + 0.865(i-1)^2]\cos(j)$$

$$y(i,j) = [3048 + 15(i-1) + 0.865(i-1)^2]\sin(j) \quad (38)$$

where $x(i, j)$ and $y(i, j)$ are grid point coordinates at (i,j); $i = 1,2,\ldots,52$ and $j = 1,2,\ldots,361$ (where the argu-

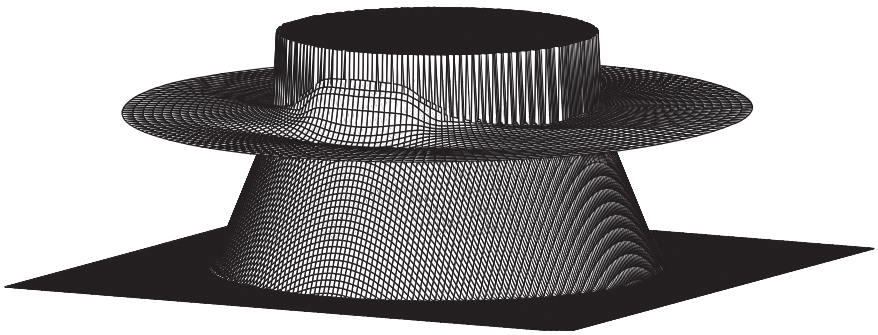

Fig. 10. Calculated wave set-up.

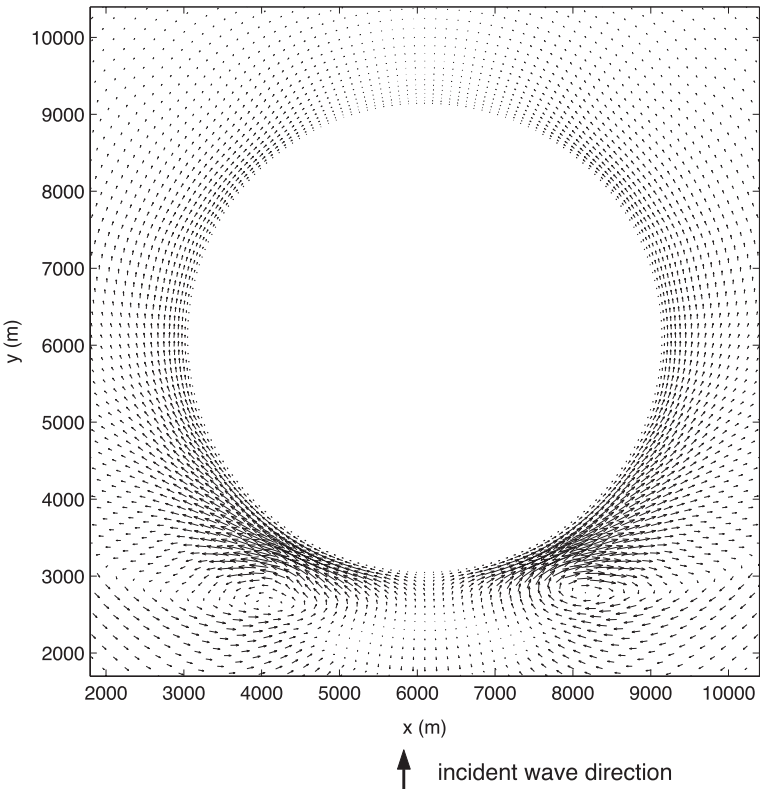

Fig. 11. Vectors of volume flux calculated from the numerical model.

ment of the sine and cosine is assumed to be degrees in Eq. (38)). The figure shows a finer grid used in the nearshore region to resolve the surf zone. The minimum grid spacing is 15.8 m in the nearshore region and the maximum is 60 m in the offshore region. Notice that there are four boundaries in the computational domain, rather than two boundaries usually used in the polar coordinates. Besides the island boundary and the offshore boundary shown in Fig. 9, there are two lateral boundaries linked on the lee

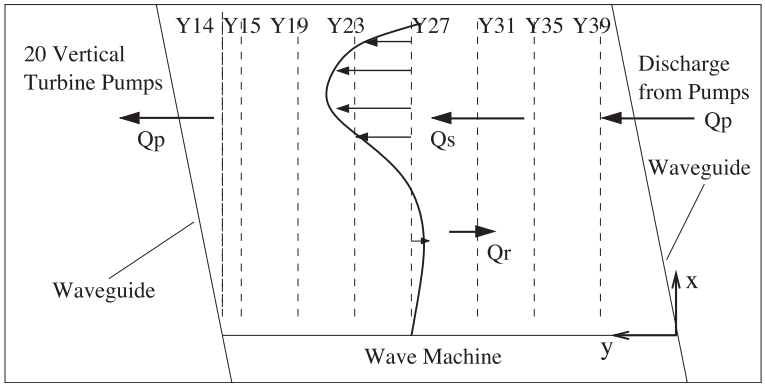

Fig. 12. Plan view of the LSTF.

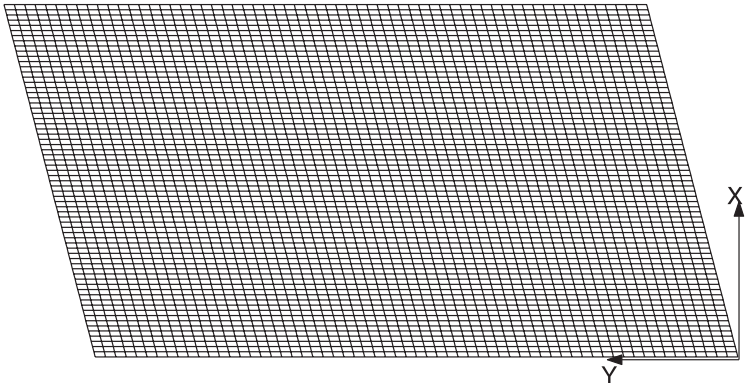

Fig. 13. Computational grid.

side along a island-normal coordinate line. Periodic boundary conditions are used at the two lateral boundaries.

Fig. 10 shows the mean surface elevation calculated from the circulation model. It is clear that a wave set-up occurs at the front shore and a slight wave set-down in the shoaling zone. The current pattern can be demonstrated by the volume flux of the calculated circulation shown in Fig. 11. There are strong longshore currents along the front shore. The currents turn back around the edges of the lee shore and complete the two cells through the shoaling zone. This result is consistent with the results of Mei and Angelides (1977). The phenomenon was thus used to explain the formation of spits protruding from the island.

4.4. Longshore current simulation in an obliquely quadrilateral domain

Recently, a longshore current experiment was carried out in the Large-scale Sediment Transport Facility (LSTF) at the U.S. Army Engineer Research and Development Center's Coastal and Hydraulics Laboratory (Hamilton and Ebersole, 2001). The LSTF has a concrete beach which has a longshore dimension of 31 m and a cross-shore dimension of 21 m, with a plane slope of 1:30. To reproduce a longshore

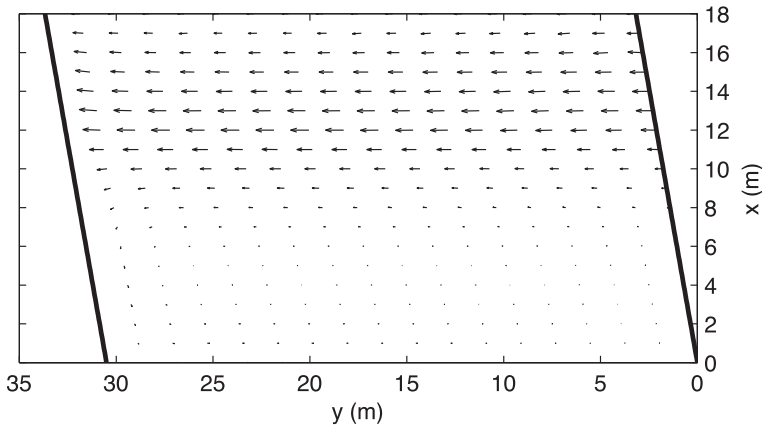

Fig. 14. Depth-averaged current velocity field.

uniform current in the finite-length wave basin, 20 independent pumps and channels are used to control the cross-shore distribution of the mean longshore current. To minimize wave diffraction into the flow channels, two obliquely oriented waveguides oriented 10° from the shoreline-normal direction were set on lateral boundaries. Fig. 12 shows a plan view of the LSTF and locations of waveguides and measurement transects (dashed lines). In the figure, Q_p is the total longshore flow rate actively pumped through the external recirculation system. If the wave-induced longshore current does not match Q_p, an internal recirculation Q_r will develop as shown in the figure. The Q_s is the total longshore flow rate between the wave set-up limit and the point of transition where the mean longshore current reverses direction. In the physical experiment, the discharge from the pumps was adjusted to minimize the internal recirculation Q_r.

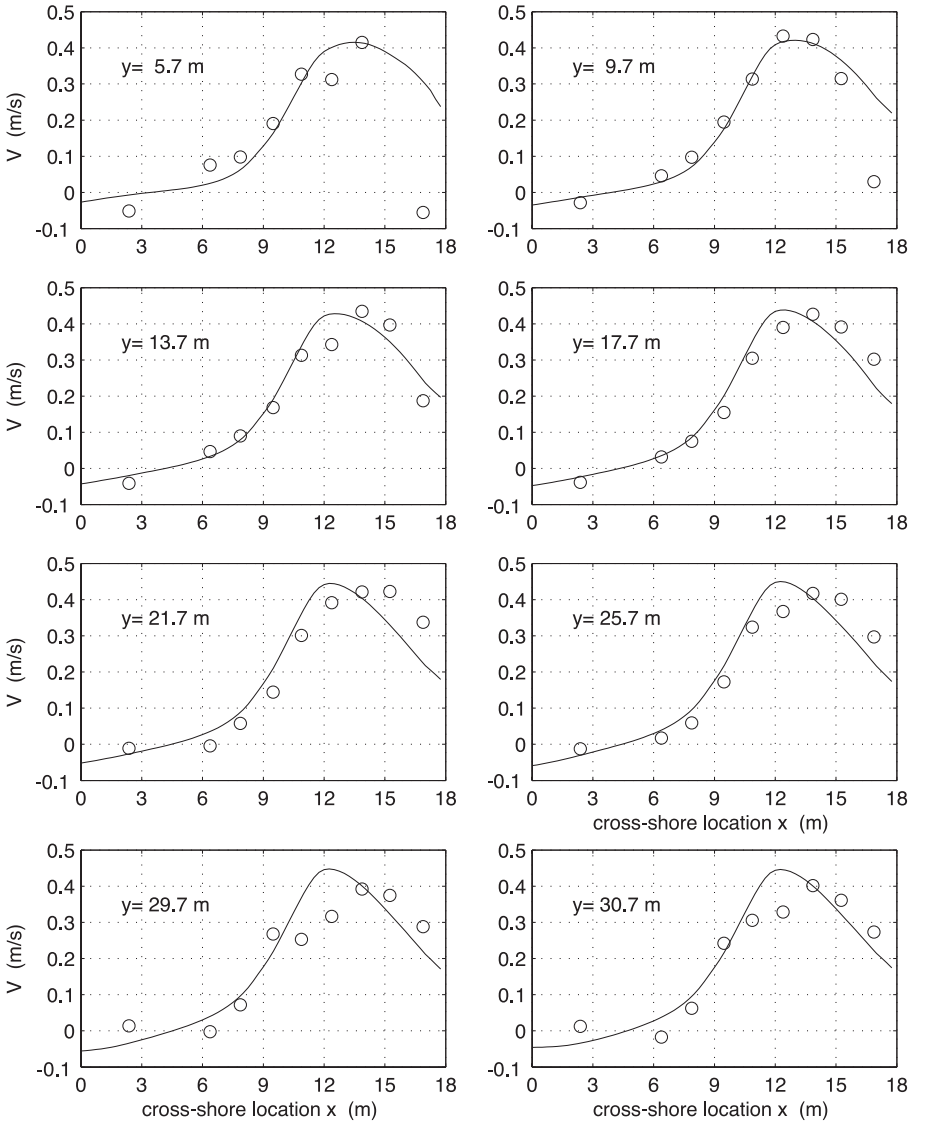

Fig. 15. Longhore current comparisons at the measurement transects (circles: measurement, solid lines: numerical results).

This technique was previously used by Visser (1980, 1984, 1991).

For the simulation of a perfect longshore uniform current without internal recirculation Q_r, the Cartesian version of SHORECIRC may be a proper model for longshore current simulations because there is no boundary effect caused by the oblique waveguides. For a more general case, however, the internal recirculation exists and the boundary effect of oblique waveguides shows up near the lateral boundaries. A boundary-fitted grid model is more appropriate for this case than a rectangular grid model. A boundary-fitted grid is generated as shown in Fig. 13. The grid sizes are 0.5 m in longshore direction and 0.26 m along the waveguide direction (0.25 m between two adjacent longshore-direction grid lines).

Again we use REF/DIF-1 as the wave-driver in a subroutine of the curvilinear SHORECIRC model. As a specified volume flux boundary condition, the measured flux at the lateral boundaries is employed by

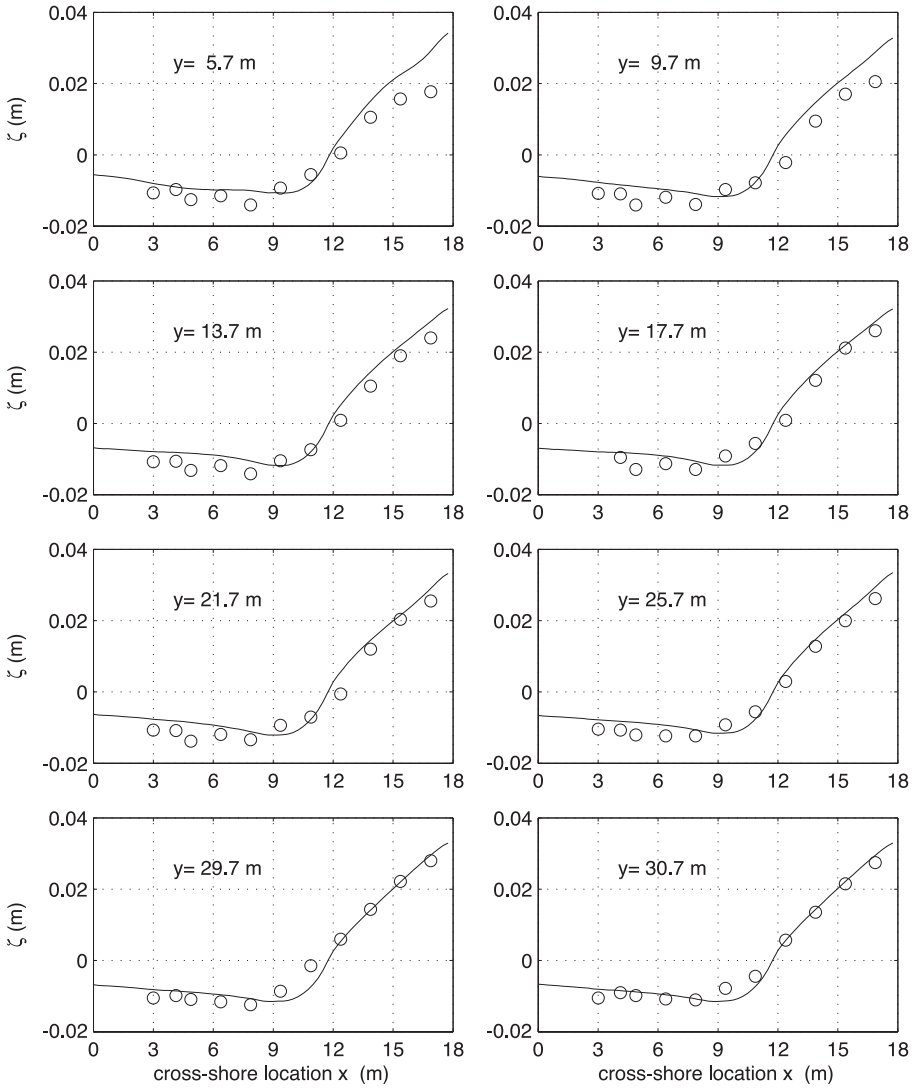

Fig. 16. Mean water level comparisons at the measurement transects (circles: measurement, solid lines: numerical results).

interpolating the data into the model boundary points. The offshore boundary and shoreline boundary are vertical walls in this case. A regular wave case was simulated from the physical experiment with a wave period of 2.5 s, 0.182 m incident wave height and 10-degree wave angle. The water depth decreases linearly from 0.667 m at the offshore boundary to 0.002 m at the shoreline boundary. The time step used in this case is 0.05 s. Wave–current interaction is taken into account in the model by calling the wave-driver subroutine every 10 s. The model reached steady state after 200 s.

Fig. 14 shows the calculated depth-averaged current field. It shows that the steady state longshore current appears approximately longshore uniform. The peak currents are around $x = 12-15$ m in the surfzone

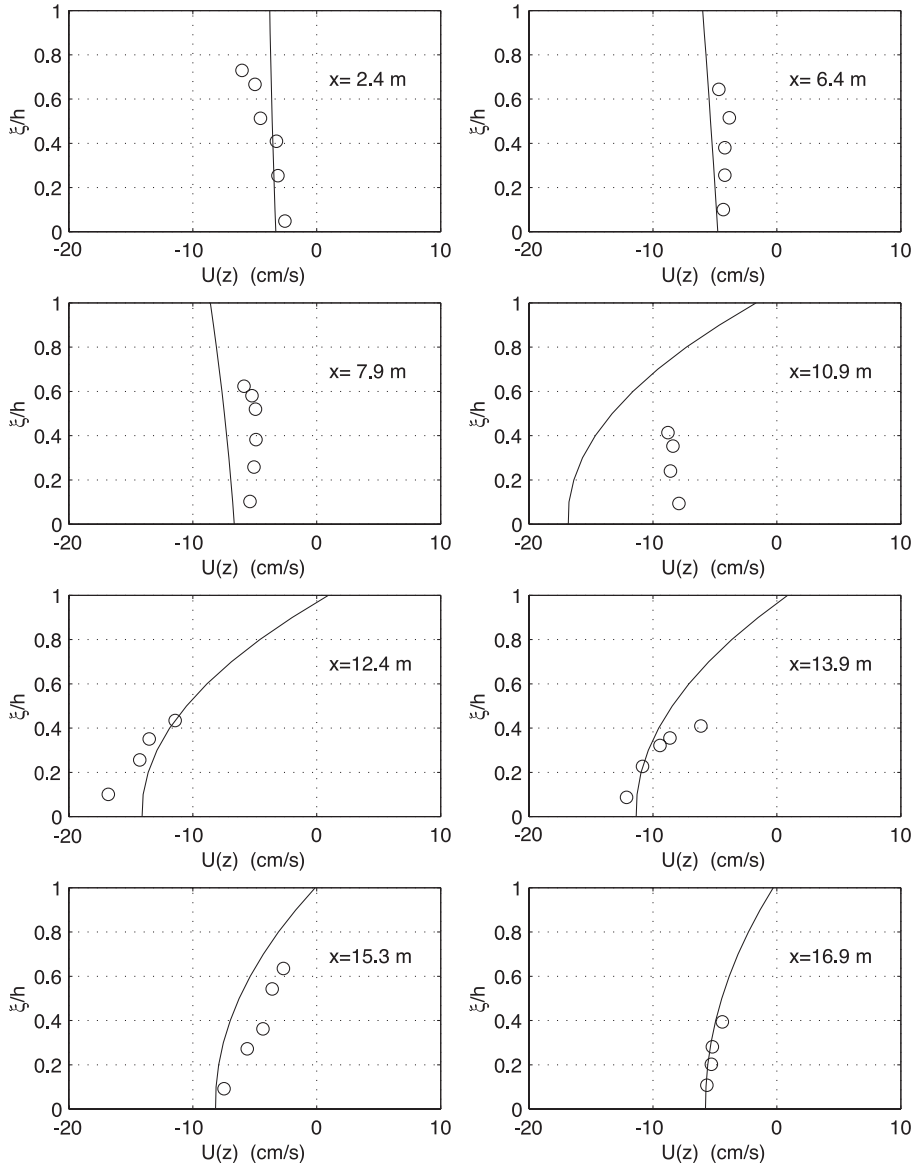

Fig. 17. Comparison of the vertical profile of cross-shore current at Y27 (circles: measurement, solid lines: numerical results).

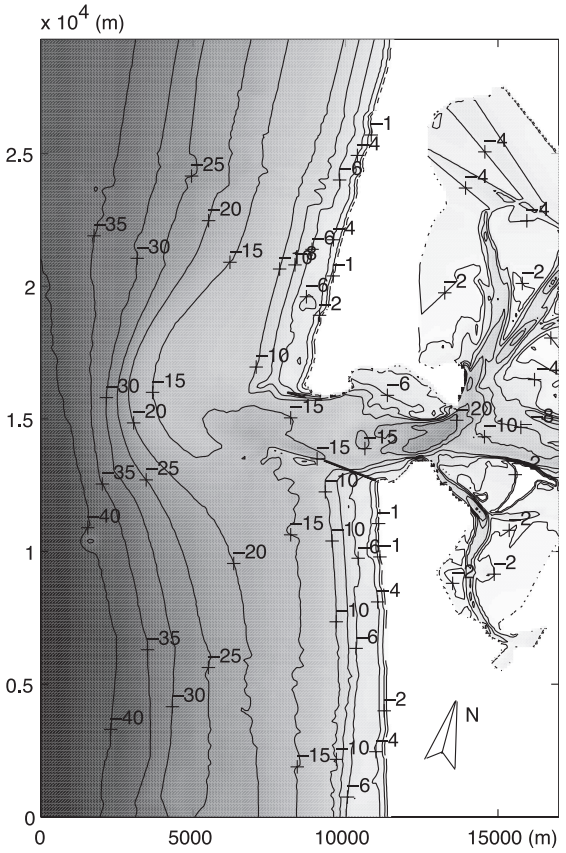

Fig. 18. Bathymetry of Grays Harbor (depths below mean tide level in meters).

while the breaking line is around $x = 9$ m in both the physical experiment and the REF/DIF-1 results. There is a very weak internal recirculation outside the surf-zone, found in the numerical results and confirmed by the experimental data.

The longshore current comparisons are made between the numerical results and experiment measurements at eight measurement transects shown by dashed lines in Fig. 12. Fig. 15 shows the comparisons, where y= 5.7, 9.7, 13.7, 17.7, 21.7, 25.7, 29.7 and 30.7 m in the figure are the model coordinates and represent the locations of the corresponding measurement transects Y39, Y35, Y31, Y27, Y23, Y19, Y15, and Y14, respectively, shown in Fig. 12. As shown in Fig. 15, the current amplitudes and the locations of peak currents are well predicted. Some apparent disagreements are found in the downstream transects of $y = 29.7$ and 30.7 m, where the measured current data show a different cross-shore variation around $x = 12$ m. This particular feature is not resolved by the model predictions. Also, an under-prediction of the currents is found near the shoreline region in the same two transects. In Fig. 16, we compare the measured mean water levels and the numerical results. The figure shows that very good agreement is obtained from the comparisons of wave set-up and set-down.

The LSTF measurements also provide information about the vertical variation of the currents. As de-

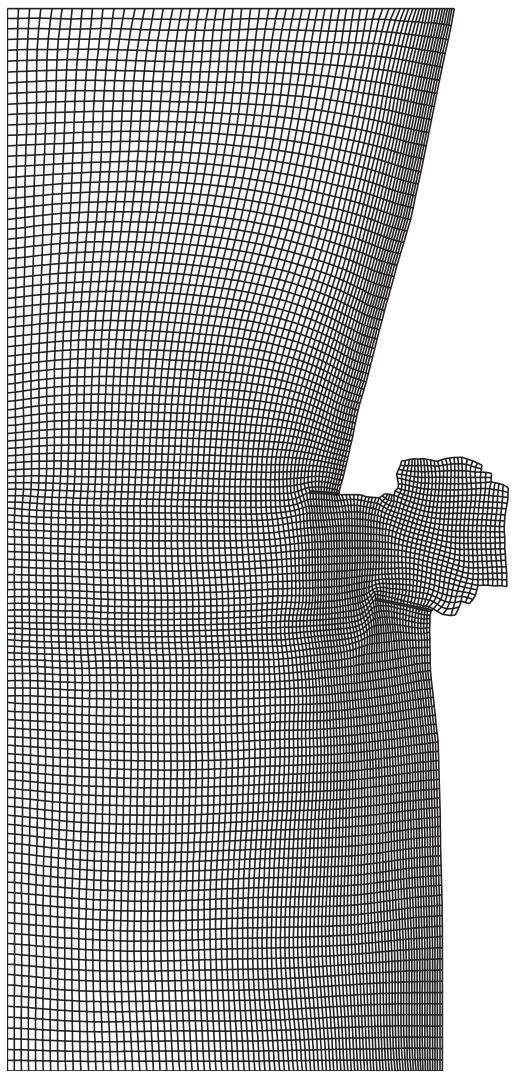

Fig. 19. Computational grid for the Grays Harbor case (Maximum grid size is 296.4 m and minimum is 59.1 m).

scribed in the model theory, the quasi-3D circulation model is able to predict the vertical profile of wave-induced current. Using Eq. (27), we can easily calculate the vertical distributions of cross-shore and alongshore velocity. Fig. 17 shows the model/data comparisons of cross-shore velocities at measurement points in transect Y27. It is shown that most of the numerical results agree well with the measurement data except the results at $x = 10.9$ m where significant deviations occur. As shown by Svendsen and Putrevu (1994) the vertical variations of the current are instrumental in providing the current lateral mixing.

4.5. Simulation of nearshore circulation at Grays Harbor

Grays Harbor is a jettied entrance on the Washington coast, located approximately 30 km north of Willapa Bay. We choose Grays Harbor as the computational domain in the case study of the curvilinear version of SHORECIRC because it includes irregular coast lines, jetties, and complicated geometry. The case illustrates the versatility of the curvilinear model to deal with complicated geometries.

Fig. 18 shows the bathymetry of Grays Harbor. There are two jetties located on the south and north side of the harbor entrance. The south jetty is approximately 1700 m long and the north jetty is about 500 m long, measured from the shoreline. The ebb shoal is offset to the north and is of low relief. The measured bathymetry does not include the water depths less than 4 m (mean tide level). Therefore the bathymetry shown in Fig. 18 is a modified version of the measured bathymetry where we extend the beach about 300 m to the shoreline using a typical beach slope of 1/80 in this region.

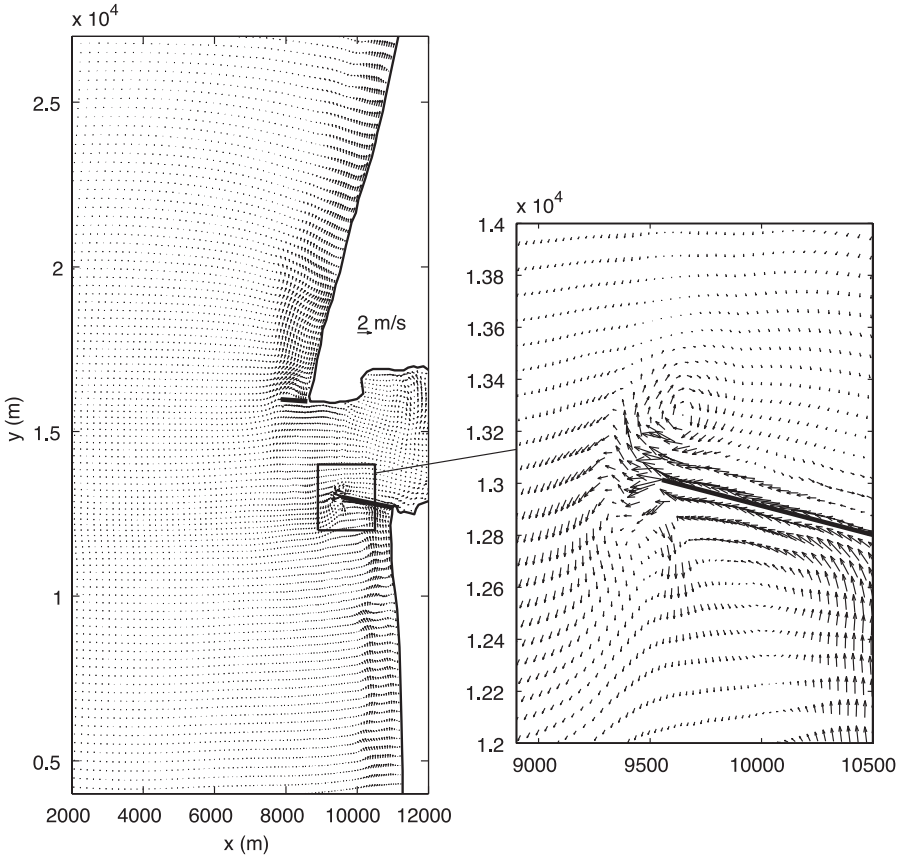

Fig. 20. Snapshot of calculated wave-induced currents ($H = 3.5$ m, $\theta = 7.5$, $T = 12$ s).

A curvilinear grid is generated using Brackbill and Saltzman's method (1982) and is shown in Fig. 19. To resolve complex nearshore bathymetry, coastlines and structures, finer resolution is used near the coastlines, jetties, and the inlet. The grid dimension is 140 × 121. The minimum grid size is 65 m near the shoreline on right side of the north jetty and maximum grid size in the offshore is about 300 m.

Several test cases are carried out using different wave conditions chosen according to the average annual storm conditions and the typical storm conditions for the site. Here we show a typical storm case with a wave height of 3.5 m and a peak wave period of 12 s. We use a monochromatic wave in REF/DIF-1 for this case. The wave direction is west-southwest, corresponding to 7.5° in the x–y coordinates of the model.

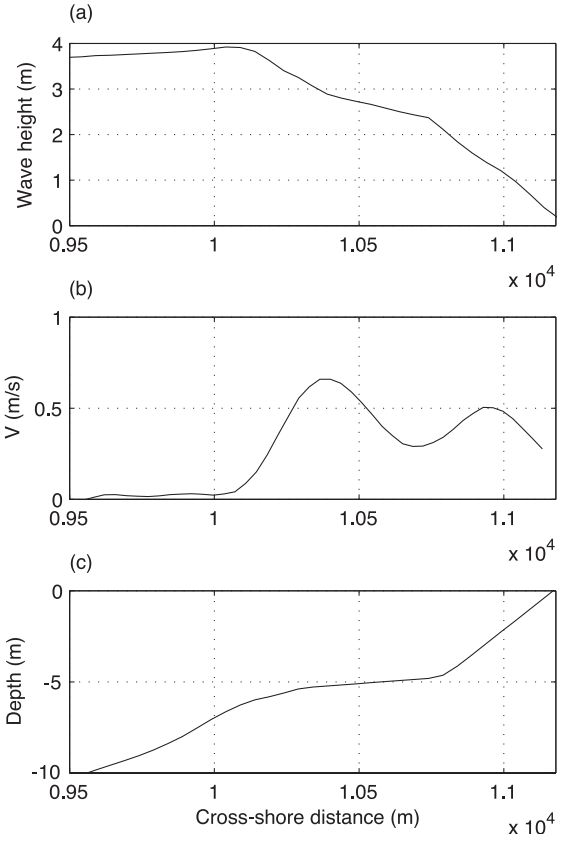

Fig. 21. Cross-shore distributions of wave height (a), longshore current (b), and water depth (c), along $y = 6561$ m.

Fig. 20 shows a snapshot of the nearshore circulation calculated from the model. Strong longshore currents develop in the surfzone. The current patterns around the two jetties are complex with vortices near the tips of the jetties. The zoom-in figure shows the complex patterns of the current near the south jetty. It should be noted that there is a broad current flowing southward near the tip of the south jetty and the cause of the flow needs to be further investigated. In the region south of the south jetty, there are two peaks of longshore currents caused by the barred beach. Fig. 21 shows a water depth profile along $y = 6561$ m and corresponding cross-shore distributions of wave height and longshore current. The current magnitude is about 1 *m/s* which is a reasonable magnitude of wave-induced currents under this wave condition (Gelfenbaum et al., 2000).

Though the numerical results have not been compared with measurements because of an absence of measurement data at this moment, this case study illustrates that the curvilinear version of SHORECIRC has a potential for computations in complicated domains. A further study of the Grays Harbor case is being carried out with considerations of wave-driven current, tidal currents and model/data comparisons and will be reported in the near future.

5. Conclusion

Using a generalized coordinate transformation and contravariant technique, curvilinear equations of the quasi-3D nearshore circulation model are derived in this paper based on the work of PS99. The curvilinear model is implemented by employing a high-order finite difference scheme and using a staggered grid in the transformed image domain. To make the model applicable to irregular shaped domains such as harbors and tidal inlets, various point types are defined in the model to recognize various boundary conditions.

The numerical convergence is tested, and very good convergence rates with both space and time discretization are obtained. The model is then used in four case studies. In the first case, a boundary-fitted curvilinear grid is used in the simulation of nearshore circulations generated on a curved beach by the diffracted waves in the lee of a breakwater. The

numerical results show very good agreement with experimental results by Gourlay (1974). The second case shows the simulation of longshore circulation around a conical island. Circulation cells are found on the sides of the island, which is consistent with Mei and Angelides (1977). The third case, longshore current simulation in an obliquely quadrilateral domain, uses a non-orthogonal Cartesian grid to fit obliquely oriented wave guides used in the LSTF laboratory experiment by Hamilton and Ebersole (2001). The model/data comparisons of the longshore current, wave set-up, as well as vertical profile of cross-shore current show the accuracy of the curvilinear model. The simulation of nearshore circulation at Grays Harbor, as the last case, illustrates the capability of the model in dealing with irregular geometries in complicated domains. For this case no measured data is available. Compared to the Cartesian version of the nearshore circulation model which is only used in rectangular domains, the present curvilinear version with the successful test cases shows its versatility to handle complicated geometries.

Further work with a moving shoreline boundary condition (Brocchini et al., 2002) and an absorbing-generating boundary condition (Van Dongeren and Svendsen, 1997) may be needed to deal with moving shoreline problems and non-reflecting seaward boundary problems. More practical applications of the curvilinear model, such as the Grays Harbor case, need to be investigated with field data verification. As one of the circulation components in the nearshore community model, the source code of the curvilinear version of the Quasi-3D nearshore circulation model will be available on line at http://www.coastal.udel.edu/kirby/NOPP/index.html.

Acknowledgements

This study was supported by the National Oceanographic Partnership Program (NOPP), Office of Naval Research, Coastal Dynamics Program and National Science Foundation, Physical Oceanography Program. The authors would like to express their appreciation to the U.S. Army Engineer District, Seattle, who supplied the Grays Harbor bathymetry data. In addition, we also would like to thank Michael R. Gourlay, University of Queensland, Australia, for his thoughtful suggestions and permission to employ his laboratory data. Permission to publish this paper was granted by the Chief of Engineers, U.S. Army Corps of Engineers.

Appendix A. Derivations of equations

A.1. Derivations of Eq. (6)

The variables defined in Eq. (5) can be expressed using the new basis ($\mathbf{a}_1$, $\mathbf{a}_2$, $\mathbf{k}$):

$$\mathbf{u} = u^\alpha \mathbf{a}_\alpha + w\mathbf{k}, \quad \mathbf{V} = V^\alpha \mathbf{a}_\alpha + W\mathbf{k},$$
$$\tilde{V} = \tilde{V}^\alpha \mathbf{a}_\alpha, \quad \mathbf{V}_1 = V_1^\alpha \mathbf{a}_\alpha, \tag{39}$$

$$\mathbf{u_w} = u_w^\alpha \mathbf{a}_\alpha + w_w \mathbf{k}, \quad \mathbf{u}' = u'^\alpha \mathbf{a}_\alpha + w'\mathbf{k}. \tag{40}$$

where w, w_w and w' are vertical components of instantaneous velocity, short-wave velocity and turbulence velocity, respectively. $V^\alpha = \tilde{V}^\alpha + V_1^\alpha$ and W is the vertical component of the time averaged velocity.

The depth-integrated, short-wave-averaged continuity equation may be written in a general form as

$$\frac{\partial \bar{\zeta}}{\partial t} + \mathrm{div}_H \tilde{V} = 0 \tag{41}$$

where div_H means horizontal divergence. According to tensor calculus, Eq. (41) can also be expressed in a tensor-invariant form:

$$\frac{\partial \bar{\zeta}}{\partial t} + (\tilde{V}^\alpha h)_{,\alpha} = 0 \tag{42}$$

where $()_\alpha$ is the covariant derivative of a first-order tensor. For an arbitrary vector $u^\alpha \mathbf{a}_\alpha$, for instance, its covariant derivative is defined as

$$u^\beta_{,\alpha} = \frac{\partial u^\beta}{\partial \xi_\alpha} + u^\delta \Gamma^\beta_{\alpha\delta} \tag{43}$$

Using the following expression of $\Gamma^\beta_{\alpha\delta}$

$$\Gamma^\beta_{\alpha\delta} = \frac{\partial^2 x_l}{\partial \xi_\alpha \partial \xi_\delta} \frac{\partial \xi_\beta}{\partial x_l} \tag{44}$$

Eq. (42) can be written in the form of Eq. (6).

A.2. Derivations of Eq. (9)

The depth-integrated, short-wave-averaged momentum equation is written in the generalized form as

$$\frac{\partial}{\partial t}(\tilde{V}h)+\mathrm{div}_H\left[\left(\tilde{V}^\alpha\tilde{V}^\beta h+\overline{\int_{-h_0}^{\zeta}V_1^\alpha V_1^\beta \mathrm{d}z}+\overline{\int_{\zeta t}^{\zeta}(u_w^\alpha V_1^\beta+V_1^\alpha u_w^\beta)\mathrm{d}z}\right)\mathbf{a}_\alpha\mathbf{a}_\beta\right]+\frac{1}{\rho}\mathrm{div}_H\mathbf{T}+\frac{1}{\rho}\mathrm{div}_H\mathbf{S}+gh\mathrm{grad}\zeta-\frac{1}{\rho}\tau_s+\frac{1}{\rho}\tau_B=0 \tag{45}$$

In Eq. (45), **S** and **T** represent the radiation stress and the Reynolds' stress, respectively. After the following approximation made in PS99

$$\overline{\int_{-h_0}^{\zeta}V_1^\alpha V_1^\beta \mathrm{d}z}+\overline{\int_{\zeta t}^{\zeta}(u_w^\alpha V_1^\beta+V_1^\alpha u_w^\beta)\mathrm{d}z}\approx\int_{-h_0}^{\bar{\zeta}}V_1^\alpha V_1^\beta \mathrm{d}z+V_1^\beta(\bar{\zeta})Q_w^\alpha+V_1^\alpha(\bar{\zeta})Q_w^\beta, \tag{46}$$

the simplified form of the momentum equation (PS99, Eq. (9)) is written in a tensor-invariant form as

$$\frac{\partial}{\partial t}(\tilde{V}^\alpha h)+\left(\tilde{V}^\alpha\tilde{V}^\beta h+\int_{-h_0}^{\bar{\zeta}}V_1^\alpha V_1^\beta \mathrm{d}z+Q_w^\alpha V_1^\beta(\bar{\zeta})+V_1^\alpha(\bar{\zeta})Q_w^\beta\right)_{,\beta}+\frac{1}{\rho}T_{,\beta}^{\alpha\beta}+\frac{1}{\rho}S_{,\beta}^{\alpha\beta}+gh\frac{\partial\zeta}{\partial\xi_\beta}g^{\beta\alpha}-\frac{1}{\rho}\tau_s^\alpha+\frac{1}{\rho}\tau_B^\alpha=0 \tag{47}$$

In Eq. (47), $S^{\alpha\beta}$ is the contravariant component of radiation stress which is a second-order tensor. According to the relationship between two different bases, the relationship between $S^{\alpha\beta}$ and $S_{\alpha\beta}$ can be easily obtained as:

$$S^{11}=\frac{1}{g_0}\left(S_{11}\left(\frac{\partial x_2}{\partial\xi_2}\right)^2-2S_{12}\frac{\partial x_2}{\partial\xi_2}\frac{\partial x_1}{\partial\xi_2}+S_{22}\left(\frac{\partial x_1}{\partial\xi_2}\right)^2\right) \tag{48}$$

$$S^{12}=S^{21}=\frac{1}{g_0}\left(-S_{11}\frac{\partial x_2}{\partial\xi_1}\frac{\partial x_2}{\partial\xi_2}+S_{12}\left(\frac{\partial x_1}{\partial\xi_1}\frac{\partial x_2}{\partial\xi_2}+\frac{\partial x_2}{\partial\xi_1}\frac{\partial x_1}{\partial\xi_2}\right)-S_{22}\frac{\partial x_1}{\partial\xi_1}\frac{\partial x_1}{\partial\xi_2}\right) \tag{49}$$

$$S^{22}=\frac{1}{g_0}\left(S_{11}\left(\frac{\partial x_2}{\partial\xi_1}\right)^2-2S_{12}\frac{\partial x_1}{\partial\xi_1}\frac{\partial x_2}{\partial\xi_1}+S_{22}\left(\frac{\partial x_1}{\partial\xi_1}\right)^2\right) \tag{50}$$

Usually $S_{\alpha\beta}$ is computed from a wave model and $S^{\alpha\beta}$ is then obtained using Eqs. (48)–(50). Another way to get the term $S_{,\beta}^{\alpha\beta}$ is to calculate the contravariant component of div **S** from its Cartesian components which is directly obtained from a wave model in Cartesian coordinates.

The term $T_{,\beta}^{\alpha\beta}$ in Eq. (47) is the contravariant component of Reynolds' stress which is also a second-order tensor. It can be calculated using the rate-of-strain tensor defined by

$$\mathbf{D}=\frac{1}{2}[\mathrm{grad}\tilde{V}+(\mathrm{grad}\tilde{V})^T], \tag{51}$$

and

$$\mathrm{div}\mathbf{T}=\mathrm{div}(hv_t\mathbf{D}), \tag{52}$$

where $()^T$ represents the transpose of a tensor, v_t is the diffusion coefficient. Using tensor calculus, div**T** or $T_{,\beta}^{\alpha\beta}$ is expressed as

$$T_{,\beta}^{\alpha\beta}=\frac{1}{\sqrt{g_0}}\frac{\partial\sqrt{g_0}vhD^{\alpha\beta}}{\partial\xi_\beta}+vhD^{\gamma\beta}\Gamma_{\gamma\beta}^\alpha \tag{53}$$

where

$$D^{\alpha\beta}=\frac{1}{2}(g^{\gamma\beta}u_{,\gamma}^\alpha+g^{\gamma\alpha}u_{,\gamma}^\beta) \tag{54}$$

A.3. Derivation of Eq. (12)

The general form of the horizontal momentum equation PS99 Eq. (10) reads

$$\frac{\partial\mathbf{u}_H}{\partial t}+(\mathrm{div}_H(\mathbf{uu}))_H=-\frac{\mathbf{1}}{\rho}(\mathrm{grad}\boldsymbol{p})_H \tag{55}$$

where $\mathbf{u}=\mathbf{u}_H+\mathbf{w}$, $()_H$ means a horizontal component. (div $(\mathbf{uu})$)$_H$ can be divided into two parts below.

$$(\mathrm{div}(\mathbf{uu}))_H=\mathrm{div}_H\cdot(\mathbf{u}_H\mathbf{u}_H)+(u^\alpha w)_{,z}\mathbf{a}_\alpha \tag{56}$$

where $\alpha=1,2$. Extending $(u^\alpha w)_{,z}$ and using the tensor calculus

$$(u^\alpha w)_{,z}=\frac{\partial u^\alpha w}{\partial z}+\Gamma^\alpha_{\beta 3}u^\beta w+\Gamma^3_{\beta 3}u^\alpha u^\beta=\frac{\partial u^\alpha w}{\partial z} \tag{57}$$

The derivation above used the following values of second kind Christoffel symbols

$$\Gamma^\alpha_{\beta 3}=\Gamma^3_{\beta 3}=0 \tag{58}$$

Then (56) can be written as

$$(\mathrm{div}(\mathbf{uu}))_H=\mathrm{div}_H(\mathbf{u}_H\mathbf{u}_H)+\frac{\partial u^\alpha w}{\partial z}\mathbf{a}_\alpha \tag{59}$$

Using Eq. (59), Eq. (55) may be expressed in the tensor-invariant form as shown in Eq. (12)

A.4. Derivation of Eq. (14)

According to Eq. (59), the terms involving u' in Eq. (13) can be written in the general tensor form:

$$(\overline{u'^\alpha u'^\beta})_{,\beta}\mathbf{a}_\alpha+\frac{\partial}{\partial z}(\overline{u'^\alpha w'})\mathbf{a}_\alpha=(\mathrm{div}(\overline{\mathbf{u}'\mathbf{u}'}))_H \tag{60}$$

Reynolds stresses may be expressed by introducing the rate-of-strain tensor

$$\overline{\mathbf{u}'\mathbf{u}'}=-\nu_t[\mathrm{grad}\boldsymbol{V}+(\mathrm{grad}\boldsymbol{V})^T]. \tag{61}$$

Eq. (61) may be written in a tensor-invariant form as

$$\begin{aligned}\overline{\mathbf{u}'\mathbf{u}'}=&-\nu_t(g^{\gamma\beta}V^\alpha_{,\gamma}+g^{\gamma\alpha}V^\beta_{,\gamma})\mathbf{a}_\alpha\mathbf{a}_\beta\\&-\nu_t\left(g^{\gamma\alpha}\frac{\partial W}{\partial\xi_\gamma}+\frac{\partial V^\alpha}{\partial z}\right)\mathbf{k}\mathbf{a}_\alpha\\&-\nu_t\left(\frac{\partial V^\alpha}{\partial z}+g^{\gamma\alpha}\frac{\partial W}{\partial\xi_\gamma}\right)\mathbf{a}_\alpha\mathbf{k}\end{aligned} \tag{62}$$

where $(\alpha,\ \beta,\ \gamma)=1,2$. The above derivation used the values of contravariant metric:

$$\begin{aligned}g^{3\alpha}&=g^{\alpha 3}=0\\g^{33}&=1\end{aligned} \tag{63}$$

and Christoffel symbols (Eq. (58)).

Substitution of Eq. (62) into Eq. (60) leads to the representation of (div$(\overline{\mathbf{u}'\mathbf{u}'})$)$_H$:

$$\begin{aligned}(\mathrm{div}(\overline{\mathbf{u}'\mathbf{u}'}))_H=&[-\nu_t(g^{\gamma\beta}V^\alpha_{,\gamma}+g^{\gamma\alpha}V^\beta_{,\gamma})]_{,\beta}\mathbf{a}_\alpha\\&-\frac{\partial}{\partial z}\left[\nu_t\left(\frac{\partial V^\alpha}{\partial z}+g^{\beta\alpha}\frac{\partial W}{\partial\xi_\beta}\right)\right]\mathbf{a}_\alpha\end{aligned} \tag{64}$$

Substituting Eq. (64) into Eq. (13) gives the tensor-invariant form (Eq. (14)).

Appendix B. Dispersive mixing coefficients

Using Eq. (27) and the expressions of A, B, D and M in PS99, we get

$$\begin{aligned}D_{\alpha\beta}=\frac{1}{\nu_t}\Bigg[&\frac{1}{63}d_{1\alpha}d_{1\beta}h^6+\frac{1}{36}(d_{1\alpha}e_{1\beta}+d_{1\beta}e_{1\alpha})h^5\\&+\left(\frac{1}{15}d_{1\alpha}(f_{1\beta}+f_{2\beta})+\frac{1}{15}d_{1\beta}(f_{1\alpha}+f_{2\alpha})\right.\\&\left.+\frac{1}{20}e_{1\alpha}e_{1\beta}\right)h^4+\frac{1}{8}(e_{1\alpha}(f_{1\beta}+f_{2\beta})\\&+e_{1\beta}(f_{1\alpha}+f_{2\alpha}))h^3+\frac{1}{3}(f_{1\alpha}+f_{2\alpha})(f_{1\beta}+f_{2\beta})h^2\Bigg]\end{aligned} \tag{65}$$

$$\begin{aligned}B_{\alpha\beta}=-\frac{1}{\nu_t}\Bigg[&\frac{4}{63}d_{1\beta}d_{1\alpha}h^6+\left(\frac{1}{12}d_{1\alpha}e_{1\beta}+\frac{1}{12}e_{1\alpha}d_{1\beta}\right)h^5\\&+\left(\frac{2}{15}d_{1\alpha}(f_{1\beta}+f_{2\beta})+\frac{2}{15}d_{1\beta}(f_{1\alpha}+f_{2\alpha})\right.\\&\left.+\frac{1}{10}e_{1\alpha}e_{1\beta}\right)h^4+\left(\frac{1}{8}e_{1\alpha}(f_{1\beta}+f_{2\beta})\right.\\&\left.+\frac{1}{8}e_{1\beta}(f_{1\alpha}+f_{2\alpha})\right)h^3\Bigg]\end{aligned} \tag{66}$$

$$M_{\alpha\beta} = \frac{1}{5}d_{1\alpha}d_{1\beta}h^5 + \frac{1}{4}(d_{1\alpha}e_{1\beta} + d_{1\beta}e_{1\alpha})h^4 + \frac{1}{3}(d_{1\alpha}(f_{1\beta}+f_{2\beta}) + d_{1\beta}(f_{1\alpha}+f_{2\alpha}) + e_{1\alpha}e_{2\beta})h^3 + \frac{1}{2}(e_{1\alpha}(f_{1\beta}+f_{2\beta}) + e_{1\beta}(f_{1\alpha}+f_{2\alpha}))h^2 + (f_{1\alpha}+f_{2\alpha})(f_{1\beta}+f_{2\beta})h + (Q_{w\alpha}d_{1\beta}+Q_{w\beta}d_{1\alpha})h^2 + (Q_{w\alpha}e_{1\beta}+Q_{w\beta}e_{1\alpha})h + Q_{w\alpha}(f_{1\beta}+f_{2\beta}) + Q_{w\beta}(f_{1\alpha}+f_{2\alpha}) \quad (67)$$

$$A_{\alpha\beta\delta} = -\frac{1}{v_t}\left\{\frac{1}{63}\left(\prod_{\alpha\delta}^{1} d_{1\beta}\right)h^7 + \frac{1}{36}\left[\prod_{\alpha\delta}^{1} e_{1\beta} + \left(\prod_{\alpha\delta}^{2} -2h_{,\delta}d_{1\alpha}\right)d_{1\beta}\right]h^6 + \left[\frac{1}{15}\prod_{\alpha\delta}^{1}(f_{1\beta}+f_{2\beta}) + \frac{1}{20}\left(\prod_{\alpha\delta}^{2} -2h_{,\delta}d_{1\alpha}\right)e_{1\beta} + \frac{1}{15}d_{1\beta}\left(\prod_{\alpha\delta}^{3} -h_{,\delta}e_{1\alpha}\right)\right]h^5 + \frac{1}{8}\left[\left(\prod_{\alpha\delta}^{2} -2h_{,\delta}d_{1\alpha}\right)(f_{1\beta}+f_{2\beta}) + \left(\prod_{\alpha\delta}^{3} -h_{,\delta}e_{1\alpha}\right)e_{1\beta}\right]h^4 + \frac{1}{3}\left(\prod_{\alpha\delta}^{3} -h_{,\delta}e_{1\alpha}\right) \times (f_{1\beta}+f_{2\beta})h^3 + \frac{1}{63}\left(\prod_{\beta\delta}^{1} d_{1\alpha}\right)h^7 + \frac{1}{36}\left[\prod_{\beta\delta}^{1} e_{1\alpha} + \left(\prod_{\beta\delta}^{2} -2h_{,\delta}d_{1\beta}\right)d_{1\alpha}\right]h^6 + \left[\frac{1}{15}\prod_{\beta\delta}^{1}(f_{1\alpha}+f_{2\alpha}) + \frac{1}{20}\left(\prod_{\beta\delta}^{2} -2h_{,\delta}d_{1\beta}\right)e_{1\alpha} + \frac{1}{15}d_{1\alpha}\left(\prod_{\beta\delta}^{3} -h_{,\delta}e_{1\beta}\right)\right]h^5 + \frac{1}{8}\left[\left(\prod_{\beta\delta}^{2} -2h_{,\delta}d_{1\beta}\right) \times (f_{1\alpha}+f_{2\alpha}) + \left(\prod_{\beta\delta}^{3} -h_{,\delta}e_{1\beta}\right)e_{1\alpha}\right]h^4 + \frac{1}{3}\left(\prod_{\beta\delta}^{3} -h_{,\delta}e_{1\beta}\right)(f_{1\alpha}+f_{2\alpha})h^3\right\} \quad (68)$$

where $\prod_{\alpha\delta}^{1}, \prod_{\alpha\delta}^{2}$ and $\prod_{\alpha\delta}^{3}$ are defined by

$$\prod_{\alpha\delta}^{1} = d_{1\alpha,\delta} + \Gamma_{k\delta}^{\alpha}d_{1k} \quad (69)$$

$$\prod_{\alpha\delta}^{2} = e_{1\alpha,\delta} + \Gamma_{k\delta}^{\alpha}e_{1k} \quad (70)$$

$$\prod_{\alpha\delta}^{3} = (f_{1\alpha}+f_{2\alpha})_{,\delta} + \Gamma_{k\delta}^{\alpha}(f_{1k}+f_{2k}) \quad (71)$$

Appendix C. Staggered grid arrangement and numerical scheme

A staggered grid in $\xi_1 - \xi_2$ plane is employed as shown in Fig. 22, where the crosses denote ζ-points at which $\bar{\zeta}$ is computed, the circles denote $\tilde{V}^1$-points at which $\tilde{V}^1$ is computed and the squares denote $\tilde{V}^2$-points at which $\tilde{V}^2$ is computed.

The first-order spatial derivative terms are discretized to fourth-order accuracy using five-point finite-defferencing. For example, $f_{\xi 1}$ may be discretized at point j as

$$f_{\xi 1} = (f_{j-2} - 27f_{j-1} + 27f_j - f_{j+1})/(24\Delta\xi_1) + O(\delta\xi_1^4) \quad (72)$$

The fourth-order Adams–Bashforth–Moulton predictor–corrector scheme is employed to perform time updating. A sequence of time instants are defined by $t = p\ \Delta t$. Level p refers to information at the present, known time level. For the time-derivative equation written by

$$\frac{\partial f}{\partial t} = E \quad (73)$$

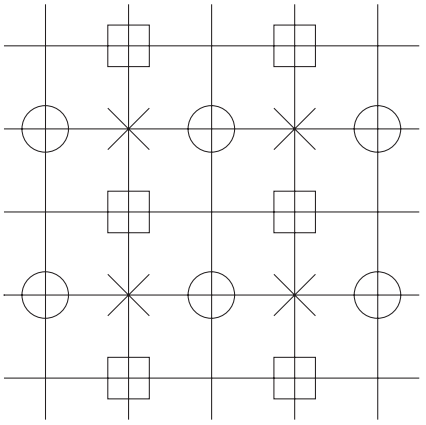

Fig. 22. Staggered grid in $\xi_1 - \xi_2$ plane ($\times\bar{\zeta}$ point, $\bigcirc - \tilde{V}^1$ and $\square - \tilde{V}^2$).

the predictor step is the third-order explicit Adams–Bashforth scheme, given by

$$f_{i,j}^{p+1} = f_{i,j}^{p} + \frac{\Delta t}{12}\left[23(E)_{i,j}^{p} - 16(E)_{i,j}^{p-1} + 5(E)_{i,j}^{p-2}\right] \quad (74)$$

After predictor step we use the fourth-order Adams–Moulton corrector method:

$$f_{i,j}^{p+1} = f_{i,j}^{p} + \frac{\Delta t}{24}\left[9(E)_{i,j}^{p+1} + 19(E)_{i,j}^{p} - 5(E)_{i,j}^{p-1} + (E)_{i,j}^{p-2}\right] \quad (75)$$

Appendix D. Interpolation/extrapolation between model grids

Interpolation or extrapolation is usually employed between the curvilinear grid used for the circulation model and the rectangular grid used for wave models.

The linear interpolation/extrapolation method is used in the present paper. We assume two grid systems, grid-1 and grid-2, which can be curvilinear grids or rectangular grids. As shown in Fig. 23, the interpolation value at point A in grid-1 is evaluated by the values at three points, 1, 2 and 3, of a triangle in grid-2 which surrounds point A. For extrapolation, point A is out of the triangle. Four triangle areas $S_{\alpha\beta\gamma}$, i.e., S_{123}, S_{12A}, S_{31A} and S_{23A} are calculated using the following formula:

$$S_{\alpha\beta\gamma} = \begin{vmatrix} x_\alpha & y_\alpha & 1 \\ x_\beta & y_\beta & 1 \\ x_\gamma & y_\gamma & 1 \end{vmatrix} \quad (76)$$

where (x_α, y_α) represents coordinates of point 1, 2, 3 and A. For interpolation, (α, β, γ) are anti-clockwise for all the four triangles and thus $S_{\alpha\beta\gamma}$ are positive. For extrapolation, clockwise (α, β, γ) results in negative $S_{\alpha\beta\gamma}$. The following formula is used for both interpolation and extrapolation:

$$F_A = (F_1 S_{23A} + F_2 S_{31A} + F_3 S_{12A})/S_{123} \quad (77)$$

where F_1, F_2, F_3 and F_A represent any converted variables at point 1, 2, 3 and A, respectively.

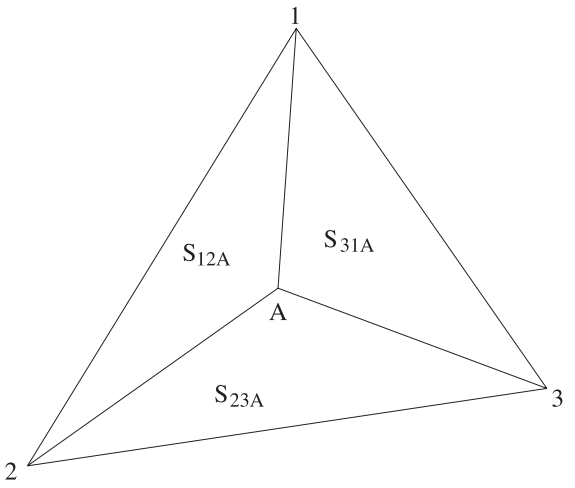

Fig. 23. Interpolation triangle.

It should be mentioned that the extrapolation is usually used at domain boundaries and is only suitable for the case that domain boundaries are close to each other. For the cases that two domain boundaries are not close to each other, e.g., Gourlay's experiment and conical island case, we make the interpolation in the overlapped region of the two grids. To save computational time for interpolation/extrapolation, $S_{\alpha\beta\gamma}$ are stored when the interpolation/extrapolation subroutine is first called.

References

Blumberg, A.F., Mellor, G.L., 1987. A description of a three-dimensional coastal ocean circulation model. In: Heaps, N. (Ed.), Three-Dimensional Coastal Ocean Models. American Geophysical Union, Washington, DC, p. 208.

Borthwick, A.G.L., Barber, R.W., 1992. River and reservoir flow modeling using the transformed shallow water equations. Int. J. Numer. Methods Fluids 14, 1193–1217.

Brackbill, J.U., Saltzman, J.S., 1982. Adaptive zoning for singular problems in two dimensions. J. Comput. Phys. 46, 342–368.

Brocchini, M., Svendsen, I.A., Prasad, R., Bellotti, G., 2002. A comparison of two different types of shoreline boundary conditions. J. Comput. Methods Appl. Mech. Eng. 191, 4575–4596.

Gelfenbaum, G., Sherwood, C.R., Kerr, L.A., Kurrus, K., 2000, Grays Harbor wave refraction experiment 1999: data report, Open-File Report 00-404, U.S. Geological Survey.

Gourlay, M.R., 1974. Wave set-up and wave generated currents in the lee of a breakwater or headland. Proc. 14th Coastal Eng. Conf., Copenhagen, 1976–1995.

Haas, K., Svendsen, I.A., Haller, M.C., 1998. Numerical modeling

of nearshore circulation on a barred beach with rip channels. Proc. 26th Int. Conf. on Coast. Eng., Copenhagen, pp. 801–814.
Hamilton, D.G., Ebersole, B.A., 2001. Establishing uniform longshore currents in a large-scale sediment transport facility. Coast. Eng. 42, 199–218.
Häuser, J., Paap, H.G., Eppel, D., Mueller, A., 1985. Solution of shallow water equations for complex flow domains via boundary fitted coordinates. Int. J. Numer. Methods Fluids 5, 727–744.
Häuser, J., Paap, H.G., Eppel, D., Sengupta, S., 1986. Boundary conformed coordinate systems for selected two-dimensional fluid flow problems: Part 2. Application of the BFG method. Int. J. Numer. Methods Fluids 6, 529–539.
Kirby, J.T., Dalrymple, R.A., 1986. Modeling waves in surfzones and around islands. J. Waterw., Port, Coast., Ocean Eng. 112, 78–93.
Kirby, J.T., Dalrymple, R.A., Shi, F., 2002. Combined Refraction/Diffraction Model REF/DIF 1, Version 2.6. Documentation and User's Manual, Research Report No.CACR-02-02. Center for Applied Coastal Research, Department of Civil and Environmental Engineering. University of Delaware, Newark.
Mei, C.C., Angelides, D., 1977. Longshore circulation around a conical island. Coast. Eng. 1, 31–42.
Putrevu, U., Svendsen, I.A., 1995. Vertical structure of the undertow outside the surf zone. Eur. J. Mech. 18 (1999) 409–427.
Putrevu, U., Svendsen, I.A., 1999. Three-dimensional dispersion of momentum in wave-induced nearshore currents. Eur. J. Mech., 83–101.
Raghunath, R., Sengupta, S., Häuser, J., 1987. A study of the motion in rotating containers using a boundary-fitted coordinate system. Int. J. Numer. Methods Fluids 7, 453–464.
Sancho, F.E., Svendsen, I.A., 1998. Shear waves over longshore nonuniform barred beaches. Proc. 26th Int. Conf. on Coast. Eng., Copenhagen, pp. 230–243.
Sancho, F.E., Svendsen, I.A., Van Dongeren, A.R., Putrevu, U., 1995. Longshore nonuniformities of nearshore currents. Coastal Dynamics'95, Gdansk, 425–436.
Sheng, Y.P., 1986. Modeling coastal and estuarine processes using boundary-fitted grids. Proceedings 3rd Int'l Symposium on River, 1416–1442.
Shi, F., Sun, W., 1995. A variable boundary model of storm surge flooding in generalized curvilinear coordinate grids. Int. J. Num. Methods Fluids 21, 641–651.
Shi, F., Sun, W., Wei, G., 1997. A WDM method on generalized curvilinear grid for calculation of storm surge flooding. Appl. Ocean Res. 19, 275–282.
Shi, F., Dalrymple, R.A., Kirby, J.T., Chen, Q., Kennedy, A., 2001. A fully nonlinear Boussinesq model in generalized curvilinear coordinates. Coast. Eng. 42, 237–258.
Smith, R., 1997. Multi-mode models of flow and of solute dispersion in shallow water: Part 3. Horizontal dispersion tensor for the velocity. J. Fluid Mech. 352, 331–340.
Svendsen, I.A., Haas, K., 1999. Interaction of undertow and rip currents. Proc. 5th Int. Conf. Coastal and Port Engrg. Developing Countries, Cape Town, pp. 218–229.
Svendsen, I.A., Putrevu, U., 1994. Nearshore mixing and dispersion. Proc. Roy. Soc. Lond. A 445, 561–576.
Svendsen, I.A., Sancho, F.E., Oltman-Shay, J., Thornton, E.B., 1997. Modelling nearshore circulation under field conditions. Proceedings Waves'97 Conference, Virginia Beach, 765–776.
Svendsen, I.A., Haas, K., Zhao, Q., 2000. Quasi-3D nearshore circulation model, SHORECIRC, Version 1.3.6, Report, Center for Applied Coastal Research. University of Delaware, Newark.
Taylor, G.I., 1953. Dispersion of soluble matter in solvent flowing slowly through a tube. Proc. R. Soc. Lond. A 219, 186–203.
Taylor, G.I., 1954. The dispersion of matter in a turbulent flow through a pipe. Proc. R. Soc. Lond. A 219, 446–468.
Van Dongeren, A.R., Svendsen, I.A., 1997. An absorbing-generating boundary condition for shallow water models. J. Waterw., Port, Coast., Ocean Eng. 123, 303–313.
Van Dongeren, A.R., Svendsen, I.A., 2000. Nonlinear and 3D effects in leaky infragravity waves. Coast. Eng. 41, 467–496.
Van Dongeren, A.R., Svendsen, I.A., Sancho, F.E., 1995. Application of the Q-3D SHORECIRC model to surfbeat. Coastal Dynamics'95, Gdansk, 233–244.
Van Dongeren, A.R., Svendsen, I.A., Sancho, F.E., 1996. Generation of infragravity waves. Proc. 25th Int. Conf. on Coast. Eng., Orlando, pp. 1335–1348.
Van Dongeren, A.R., Svendsen, I.A., Putrevu, U., 1998. Quasi 3-D effects in leaky infragravity waves. Proc. 26th Int. Conf. on Coast. Eng., Copenhagen, pp. 1323–1336.
Visser, P.J., 1980. Longshore current flows in a wave basin. Proc. 17th Int. Conf. on Coast. Eng., Sydney, pp. 462–479.
Visser, P.J., 1984. Uniform longshore current measurements and calculations. Proc. 19th Int. Conf. on Coast. Eng., Houston, pp. 2192–2207.
Visser, P.J., 1991. Laboratory measurements of uniform longshore currents. Coast. Eng. 15, 563–593.
Warsi, Z.U.A., 1998. Fluid Dynamics: Theoretical and Computational Approaches, 2nd ed. CRC Press, New York.
Wei, G., Kirby, J.T., 1995. A time-dependent numerical code for the extended Boussinesq equations. J. Waterw., Port, Coast., Ocean Eng. 121 (5), 251–261.
Winer, H.S., 1988. Numerical modeling of wave-induced currents using a parabolic wave equation. PhD dissertation, University of Florida, Gainesville.